Final Report
UM/THL-18-05

Tritium Mitigation/Control for Advanced Reactor System

Award Identification Number: The U.S. Department of Energy, DE-NE0000699

Period of Performance: 01/13/2014 to 12/31/2017

Principal Investigators
Richard Christensen, Xiaodong Sun, and Piyush Sabharwall

Submitted by

Richard Christensen
Department of Mechanical and Aerospace Engineering, The Ohio State University
Columbus, OH 43210

Xiao Wu, Shanbin Shi, and Xiaodong Sun
Department of Nuclear Engineering and Radiological Sciences, University of Michigan
Ann Arbor, MI 48109

Piyush Sabharwall
Idaho National Laboratory
Idaho Falls, ID 83415

Supported by

Nuclear Energy University Programs
The Department of Energy

May 2, 2018

FINAL REPORT

TRITIUM MITIGATION/CONTROL FOR ADVANCED REACTOR SYSTEM

by

Richard Christensen
The Ohio State University

Xiao Wu, Shanbin Shi, and Xiaodong Sun
University of Michigan

Piyush Sabharwall
Idaho National Laboratory

May 2, 2018

Prepared for

Nuclear Energy University Program
The U.S. Department of Energy

Acknowledgements

This research was performed using funding received from the U.S. Department of Energy (DOE) Office of Nuclear Energy's Nuclear Energy University Programs (NEUP). The computer simulations presented in this report were partially supported by the Ohio Supercomputer Center (OSC). The authors would like to thank Dr. David Holcomb of the Oak Ridge National Laboratory for his insightful comments and valuable suggestions throughout this project.

Executive Summary

A tritium removal facility, which is similar to the design used for tritium recovery in fusion reactors, is proposed in this study for fluoride-salt-cooled high-temperature reactors (FHRs) to result in a two-loop FHR design with the elimination of an intermediate loop. Using this approach, an economic benefit can potentially be obtained by removing the intermediate loop, while the safety concern of tritium release can be mitigated. In addition, an intermediate heat exchanger (IHX) that can yield a similar tritium permeation rate to the production rate of 1.9 Ci/day in a 1,000 MWe PWR needs to be designed to prevent the residual tritium that is not captured in the tritium removal system from escaping into the power cycle and ultimately the environment. The main focus of this study is to aid the mitigation of tritium permeation issue from the FHR primary side to significantly reduce the concentration of tritium in the secondary side and the process heat application side (if applicable). The goal of the research is to propose a baseline FHR system without the intermediate loop. The specific objectives to accomplish the goals are:

1. To estimate tritium permeation behavior in FHRs;
2. To design a tritium removal system for FHRs;
3. To meet the same tritium permeation level in FHRs as the tritium production rate of 1.9 Ci/day in 1,000 MWe PWRs;
4. To demonstrate economic benefits of the proposed FHR system via comparing with the three-loop FHR system.

The objectives were accomplished by designing tritium removal facilities, developing a tritium analysis code, and conducting an economic analysis. In the fusion reactor community, tritium extraction has been widely investigated and researched. Borrowing the experiences from the fusion reactor community, a tritium control and mitigation system was proposed. Based on mass transport theories, a tritium analysis code was developed, and the tritium behaviors were analyzed using the developed code. Tritium removal facilities were designed and laboratory-scale experiments were proposed for the validation of the proposed tritium removal facilities.

The summary of these activities conducted and the resulting outcomes are as follows:

1. A tritium control and mitigation system is designed. The system consists of four major components: a redox control strategy, a cross-flow tritium removal facility, a double-wall intermediate heat exchanger and a tritium permeation barrier coatings applied to structural materials;
2. A cross-flow tritium removal facility is designed and validation experiments are planned;
3. The intermediate heat exchanger is redesigned with a double-wall configuration to minimize tritium permeation from the primary loop into the secondary loop;
4. Tritium permeation barrier coatings are proposed to be applied to structural materials as necessary;
5. A logarithmic mean square root of partial pressure difference method is developed for mass transfer calculation for diatomic gas diffusion in metals; and
6. An economic analysis is performed to compare the two-loop and three-loop FHR designs and the results show that by eliminating the intermediate loop, the two-loop design holds economic advantages.

Table of Contents

List of Figures

List of Tables

1. Introduction

The Fluoride salt-cooled High-temperature Reactor (FHR) is a reactor concept that combines advantages of the Sodium Fast Reactor (SFR) and the High-Temperature Gas-cooled Reactor (HTGR) [1]. FHR uses the graphite-matrix coated-particle fuels proposed for the HTGRs as well as a Direct Reactor Auxiliary Cooling System (DRACS) for passive decay heat removal. The primary coolant is generally FLiBe (a mixture of LiF and BeF_2) with a melting point of 459°C and a boiling point of 1433°C. FLiBe has a specific heat capacity of 2.34 kJ/kg-K and a thermal conductivity of 1.0 W/m-K at 600°C [2]. These properties are comparable to 5.5 kJ/kg-K and 0.56 W/m-K, respectively, for water at 7.5 MPa. The FLiBe density (1,940 kg/m^3) is much higher than the density of water (732 kg/m^3) at 7.5 MPa (at saturation). Due to the low operating pressure and advantageous primary coolant characteristics (high density and good thermal characteristics) in FHRs, a significant reduction in reactor size and cost could be realized compared with high-temperature gas-cooled reactors and water-cooled reactors at a similar electricity output.

However, due to the neutron activation of the FLiBe coolant, a considerable amount of tritium is produced. This has been estimated to be 5,000 Ci/day at startup in an FHR with a power rating of 2,400 MWth [3]. Tritium formation rates (as HT or T_2) from ^{7}Li in FHRs can be comparable to the rates of HTO formation in CANDU reactors. If there is no leakage of water coolant with HTO from CANDU reactors, tritium release is not considered as an issue. However, since the gaseous form of tritium (HT or T_2) has considerable permeation rate through metal, tritium permeation issue in FHRs is more significant than that in CANDU. The tritium produced in the primary loop, if left to accumulate, has a very high permeation rate through the intermediate heat exchangers (IHXs). As a result, three-loop systems are currently being considered for FHRs in order to reduce tritium permeation to the power cycle and environment. However, the intermediate loop obviously offsets the above-mentioned benefits of the FHRs. Therefore, in this study, a tritium control and mitigation system is proposed with the attempt of eliminating the intermediate loop.

1.1 Tritium in FHRs

Tritium is of special interest among the fission products produced in advanced reactor systems, such as the FHRs. In high-temperature components, such as an IHX, tritium permeates readily in metals. The anticipated difficulty in containing tritium justifies special care in FHR system design. A sound understanding of tritium's generation pathways as well as its properties and possible ways to prevent it from escaping should be an integral part of the containment plan for FHRs.

A main source of tritium generation in the FHR core is lithium. Since highly purified lithium is used, $^{7}_{3}\mathrm{Li}$ is mainly present. Although $^{7}_{3}\mathrm{Li}$ has a small neutron absorption cross section, the number of neutron events is large [3]. On the other hand, the amount of $^{6}_{3}\mathrm{Li}$ is very small, but its neutron absorption cross section is large. Therefore, a considerable amount of tritium is produced. The major tritium producing reactions are summarized as [4]:

$$^{6}_{3}\mathrm{Li} + \mathrm{n} \rightarrow {}^{4}_{2}\mathrm{He} + {}^{3}_{1}\mathrm{H} + 4.8\ \mathrm{MeV};\ \sigma_{th} = 940\ \mathrm{b} \quad (1)$$

$$^{7}_{3}\mathrm{Li} + \mathrm{n} + 2.74\ \mathrm{MeV} \rightarrow {}^{4}_{2}\mathrm{He} + {}^{3}_{1}\mathrm{H} + \mathrm{n}';\ \sigma_{avg} = 20\ \mathrm{mb} \quad (2)$$

$$^{7}_{3}\mathrm{Li} + \mathrm{n} + 3.5\ \mathrm{MeV} \rightarrow {}^{5}_{2}\mathrm{He} + {}^{3}_{1}\mathrm{H};\ \sigma_{avg} = 20\ \mathrm{mb} \quad (3)$$

$$^{19}_{9}\mathrm{F} + \mathrm{n} + 7.56\ \mathrm{MeV} \rightarrow {}^{17}_{8}\mathrm{O} + {}^{3}_{1}\mathrm{H};\ \sigma_{avg} = 30\ \mu\mathrm{b} \quad (4)$$

where,

σ represents the absorption cross section (b: barn) for the parent nuclide;
subscript th refers to thermal neutron energies;
subscript avg refers to average neutron energies.

In the natural redox condition of the primary coolant, FLiBe, the majority of tritium generated exists in the charge state T^+ and it combines with F^- to form TF molecules. It is estimated that more than 90% of the tritium generated in the core exists in the form of TF and that the remainder exists in the form of T_2. As TF is corrosive to structure materials, it must be removed or converted to less corrosive chemicals after its generation in the core as soon as possible [3].

To prevent corrosion, it is necessary to adjust the redox condition of the primary coolant. In the fusion community, there has been a significant amount of research done in this area. The method used to maintain TF concentration at a sufficiently low level is redox control. The material used in the redox control is beryllium (Be), which reacts with HF when dissolved physically in FLiBe [5]. With the redox control, the major existence form of tritium in FHRs is T_2 dissolving in the primary coolant. Removal of T_2 from the primary loop is a process of extracting a gas solvent from a liquid solute. In the fusion community, two strategies have been investigated. The first one is a counter-current gas bubbling extraction tower, as shown in Figure 1.1.

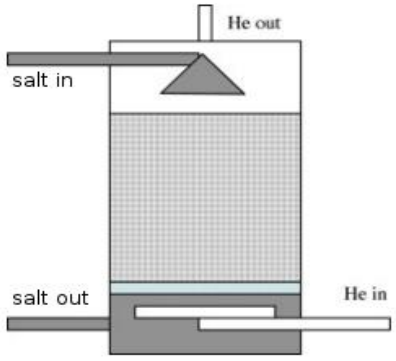

Figure 1.1 Scheme of a counter-current flow extraction tower [6]

In the counter-current extraction tower, a purge gas, such as helium, is bubbled from the bottom of the facility and through the molten salt FLiBe, which flows downward in the tower. Under the influence of helium gas bubbles, T_2 dissolved in FLiBe will convert to the gas phase and be carried away by the helium bubbles. The required size of the counter-current extraction tower can be estimated using the model developed by Fukada et al. [6]:

$$h_G = 3.07 \frac{G^{0.32}}{L^{0.51}} \left(\frac{\mu_G}{\rho_G D_G} \right)^{2/3} \quad (5)$$

$$h_L = \frac{1}{430}\left(\frac{L}{\mu_L}\right)^{0.22}\left(\frac{\mu_L}{\rho_L D_L}\right)^{0.5} \tag{6}$$

$$h = \frac{GR_g T}{k_G a_V p_T}\int_{p_{T_2,in}}^{p_{T_2,out}} \frac{dp_{T_2}}{p_{T_2,i} - p_{T_2}} \tag{7}$$

where,

h_L and h_G are called the heights equivalent to the theoretical plate of liquid-phase and gas-phase mass transfer, respectively [7];

h is the height of the counter-current extraction tower;

a_V is the total surface area of the bubbles in a unit volume. The diffusion rate through the gaseous boundary layer of the He–D_2 mixture is controlled by $k_G a_V$, which has the unit of s^{-1};

p_{T_2} is the T_2 partial pressure in the gaseous phase;

G and L are the molar flow rates of the gas phase and liquid phase, respectively;

μ is the fluid viscosity;

ρ is the density;

R_g is the ideal gas constant;

T is the temperature; and

Subscriptions G and L represent the gas phase and liquid phase, respectively.

The second method to remove tritium is use of a permeation window extraction facility. The basic scheme of the permeation window extraction facility is shown in Figure 1.2. This type of equipment is designed based on the selective permeability of metal to tritium. The permeable tube is made of a highly tritium permeable metal material. Between the permeable tube and the nonpermeable tube, a sweep gas, such as helium, helps maintain a low tritium concentration on the downstream side, i.e., the helium side, of the window. While tritium can permeate through the inner tube and be carried away by the sweep gas, other contents in the primary coolant are left inside the permeable tube [8, 9]. Therefore, tritium is extracted out of the primary loop.

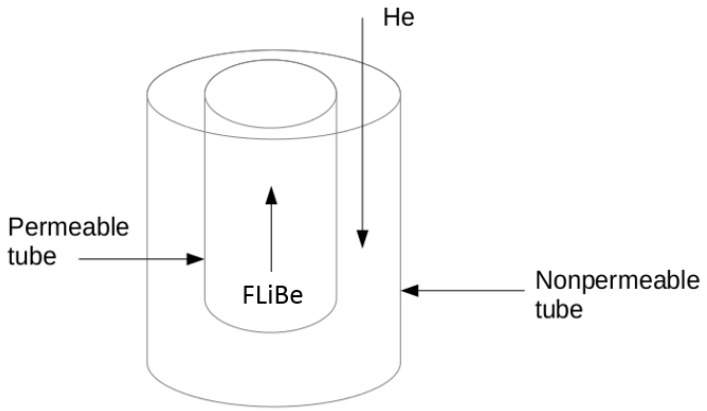

Figure 1.2 Basic scheme of a permeation window extraction facility

The total surface area needed for the permeation window can be calculated by:

$$A = \frac{Q}{k_{mt}} \frac{\ln\left(\frac{c_{\text{in}} - H_{T_2} p_2}{c_{\text{out}} - H_{T_2} p_2}\right)}{\left(c_{\text{in}} - H_{T_2} p_2\right) - \left(c_{\text{out}} - H_{T_2} p_2\right)} \tag{8}$$

where,

k_{mt} is the overall mass transfer coefficient derived from tritium diffusivities and solubilities in FLiBe, tube wall and helium;

p_2 is the partial pressure of T_2 in the downstream of the window on the helium flow side;

c_{in} and c_{out} are respectively the inlet and outlet T_2 concentrations in the upstream of the window on the liquid molten salt side, as shown in Figure 1.2.

The permeation window extraction facility brings some advantages compared to the counter-current extraction tower:

1. The permeation window extraction facility can be part of the intermediate heat exchanger. This reduces the amount of design work;
2. The purge gas is not mixed or physically in contact with the molten salt. Separate flow is more advantageous than mixed flow in the aspect of flow control;
3. The amount of helium that dissolves in the molten salt can be reduced if the material of fabrication for the permeation wall is properly selected. The permeation window material is expected to have selective permeation properties that enable T_2 to transport while allowing a negligible amount of helium to permeate through.

T_2 physically dissolves in the primary coolant, FLiBe. Therefore, the mechanism of gas transport can be applied to tritium transport in FHR systems. The permeation rate of tritium through a solid is determined by the tritium partial pressures on both sides, temperature, intrinsic properties of the material, the thickness of the solid and the surface condition. Permeability Φ is used to describe the ability of gas permeation through a solid, which is defined as the product of the diffusivity D and solubility K:

$$\underset{\text{Permeability}}{\Phi} = \underset{\text{Diffusivity}}{D} \times \underset{\text{Solubility}}{K} \tag{9}$$

Transport coefficients of hydrogen isotopes in molten salts FLiBe and FLiNaK are listed in Table 1.1. The values of the same transport coefficient of the same isotope are found to vary significantly among different research groups.

Table 1.1 Solubility values of tritium in molten salts from experiments

Gas species	Molten salt species	Solubility [mol/m^3-Pa]	Diffusivity [m^2/s]	References
T_2	FLiBe	$7.9\times10^{-2}\exp\left(-\frac{35000}{R_gT}\right)$	$9.3\times10^{-7}\exp\left(-\frac{42000}{R_gT}\right)$	[10]
H_2	FLiBe	1.13×10^{-3} (at 773 K) 3.17×10^{-3} (at 873 K) 3.87×10^{-3} (at 973 K)		[11]
D_2	FLiBe	3.1×10^{-4} (at 873 K) 1.0×10^{-4} (at 973 K)	8.0×10^{-10} (at 873 K) 3.0×10^{-9} (at 923 K)	[12]
H_2	FLiNaK	$3.98\times10^{-7}\exp\left(\frac{34400}{R_gT}\right)$	$8.69\times10^{-10}\exp\left(-\frac{50000}{R_gT}\right)$	[13]
H_2	FLiNaK	$7.06\times10^{-5}\exp\left(-\frac{54900}{R_gT}\right)$	$1.67\times10^{-7}\exp\left(-\frac{27000}{R_gT}\right)$	[14]

Tritium permeability values in some common structural materials are listed in Table 1.2.

Table 1.2 Tritium permeability in structural materials

	Permeability [mol/m-s-Pa$^{0.5}$]	References
Incoloy-800	$2.4\times10^{-10} - 5.5\times10^{-10}$	[15]
Incoloy-600	6.6×10^{-10}	[15]
SS 304L	1.2×10^{-10}	[15]
Hastelloy N	4.2×10^{-10}	[15]
Nickel alloy	9.3×10^{-10}	[15]

These values of tritium transport coefficients are used in design of the tritium removal and mitigation system and facilities, as well as in tritium transport simulation and modeling.

1.2 Tritium control and mitigation system for FHR systems

Based on the behavior of tritium in FHR systems, a tritium control and mitigation system has been designed. The system consists of a redox control facility, a tritium removal facility, and an intermediate heat exchanger (IHX) with tritium permeation barrier, as shown in Figure 1.3. Also, the tritium removal facility has an additional loop to collect tritium in the purging gas, which extracts tritium from the primary coolant. The barrier cleaning section coupled with the IHX cleans up the tritium

permeation barrier in the IHX. Each component will be discussed in more details in the following sections.

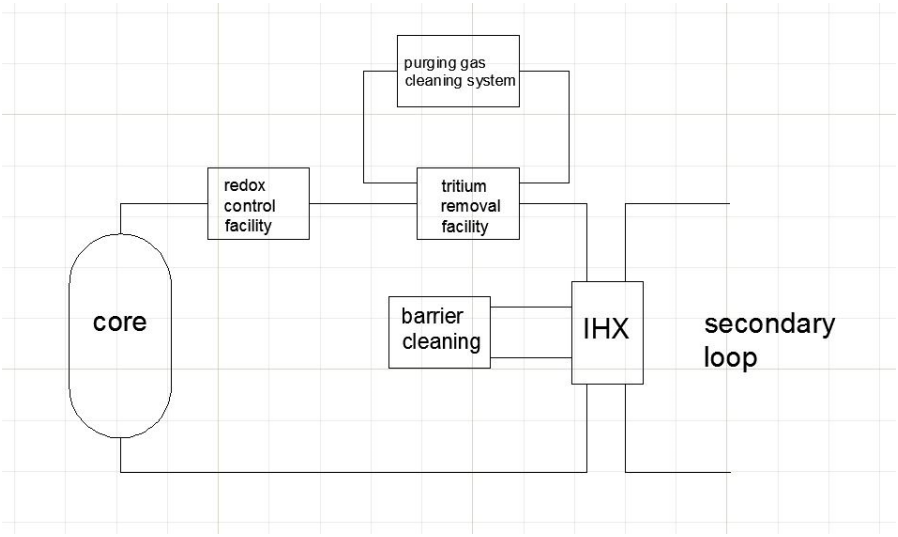

Figure 1.3 Schematic of the tritium control and mitigation system

2. Tritium Removal Facility

The tritium removal facility is located downstream of the outlet of the core, and extracts T_2 out of the primary coolant. Several designs of the tritium removal facility were proposed and simulation of each design was performed, as described in the following sections. The underlying principles for designing such a tritium removal facility are:

1. To increase the mass transfer area to volume ratio;
2. To increase the turbulence of the molten salt flow, so that the gradient of T_2 concentration from the center of the flow channel to the diffusion boundary can be flattened, reducing the diffusion resistance of T_2 in the molten salt.

2.1 Helium gas purging method

In this design, helium gas bubbles are injected into the molten salt from the bottom of the salt container, and rise due to the gas injection inertia and buoyancy, extracting T_2 molecules that are dissolved in the molten salt in the process. The molten salt can be stagnant, flowing upward or downward. However, to maximize the extraction efficiency, the salt and gas bubbles were arranged to flow counter-current. In this way, similar to a counter-current heat transfer scenario, the difference of the tritium concentration in the molten salt and the purging gas can be maximized.

Helium is selected as the purging gas mainly because of its chemical stability under high temperatures, as well as its availability and accessibility. In order to minimize heat loss to the purging gas, helium will be heated up to the molten salt core outlet temperature before being injected into the system.
A two-dimensional (2-D) model was built to evaluate the efficiency of this design and determine the required bubble sizes and number concentrations. A modified form of the COMSOL model "Packed Bed Reactor" [16] was used in the study. FLiNaK was used as the molten salt and helium as the purging gas (namely, the rising bubbles) in the simulation. For the diffusing gas, H_2 was used as a surrogate instead of T_2 because of the limited data of T_2 transport behavior.

The geometrywas modeled as a simple square, as shown in Figure 2.1, with the *x* axis representing the height of the facility and the *y* axis representing the radius dimension of a single helium bubble. The reactor model and bubble model were coupled through the flux of H_2 being transported between the two phases. This flux was given as a chemical reaction rate, calculated based on the total surface area of bubbles per unit mixture volume, i.e., the interfacial area concentration. By equating the H_2 flux leaving FLiNaK to that entering a single helium bubble, and taking into account the diffusion of H_2 in the bubble, the model ensures the mass balance of H_2.

Figure 2.1 Implicit 2-D model

Calculations showed that when the helium spherical bubbles are 2 mm in diameter and occupy a 50% or higher ratio of the total volume of the molten salt flow path, the facility can give a satisfactory tritium removal rate. However, normal bubbly flow can only contain less than 15-20% volume fraction

of bubbles (void fraction) before the bubbles start to collide and merge, decreasing the mass transfer surface area. Therefore, in the COMSOL simulations, the bubble volume fraction was set at 10% and the diameter of the bubble was 1 mm. The molten salt flow velocity was 0.2 m/s. This setup takes into consideration of the practical gas bubble volume fraction. The simulation results show that the performance of a 200-meter-long column drops after operating for 400 seconds. Considering the total amount of molten salt used in the primary loop, the current setup requires very large dimensions. Since in a bubbly flow column, to maintain the required mass transfer surface area per unit volume is a challenging task, a more practical design is sought next.

2.2 Stainless steel packed bed scrubber

Considering the practical difficulty of the purging gas method, we developed a modified design where stainless steel 304 balls replace the gas bubbles in the molten salt. In this stainless steel packed bed scrubber method, the stainless steel balls act as the collector of T_2. The use of metal balls avoids the bubble coalescence issue. Therefore, the mass transfer surface area to volume ratio can be maintained at a relatively high level. When the concentration of T_2 inside a stainless steel ball increases, its ability of absorbing T_2 will decrease accordingly. When the T_2 concentration in the stainless steel ball reaches a limiting concentration, it will need to be removed from the molten salt. For simplicity in this report, this situation is referred to as the "saturation" of the stainless steel ball, though the T_2 concentration in the stainless steel ball has not yet reached its real solubility limit. The stainless steel balls can be stagnant or circulating. As the number of stainless steel balls needed is large, they will be removed from the salt after reaching saturation, cleaned up to remove the tritium and recycled.

Graphite spheres are also considered in the design in addition to the stainless steel balls. However, since the T_2 diffusivity in graphite is nearly one fifth of that in stainless steel 304, it is theoretically less effective to use graphite spheres than to use stainless steel balls in this application. Additionally, since graphite has a moderating effect on neutrons, its influence on the reactor should be carefully evaluated before it can be used as a tritium absorption material.

A COMSOL model is built to calculate the effectiveness of this stainless steel packed bed scrubber design. The geometry of the model is the same as the one used Section 2.1 for the helium gas purging design. The properties of helium are replaced by those of stainless steel 304. H_2 diffusion in stainless steel is much slower than that in helium gas bubbles. Therefore, a decrease in tritium removal efficiency from the salt is expected. A total of five models are used in the calculation, as shown in Table 2.1. The initial concentration of T_2 in the molten salt is 1.8×10^{-7} mol/m^3, which is the tritium generation concentration in AHTR preconceptual design [3]. Figure 2.2 and Figure 2.3 present the concentration distributions of H_2 in the molten salt at different times for two different models. The *x*-axis is the length of the pipe in the direction of molten salt flow.

Table 2.1 Simulation results of the stainless steel packed bed model

Model	A_{ratio}	ε	Pipe Outside Diameter [in]	Schedule	Pipe Inner Diameter [in]/[m]	r [in]/[m]	Q [m^3/s]	U [m/s]	Re (for FLiNaK/FLiBe) [10^4]	Q by AHTR design [m^3/s]	Total length of pipe needed [m]
D20S40a	30	0.4	20	40	18.814/ 0.4779	0.309/ 0.0075	0.5	6.975	7/3.625	5.54	2200
D20S40b	30	0.4	20	40	18.814/ 0.4779	0.309/ 0.0075	0.125	1.7425	1.75/1.53		8800
D20S40c	956	0.4	20	40	18.814/ 0.4779	0.0984/ 0.0025	0.125	1.7425	0.6/0.302		8800
D36S40a	10	0.4	36	40	34.5/ 0.8763	1.74/ 0.0442	0.125	0.5175	1.0513/ 0.5229		8800
D36S40b	175	0.4	36	40	34.5/ 0.8763	0.0984/ 0.0025	0.125	0.5175	0.0803/ 0.0985		8800

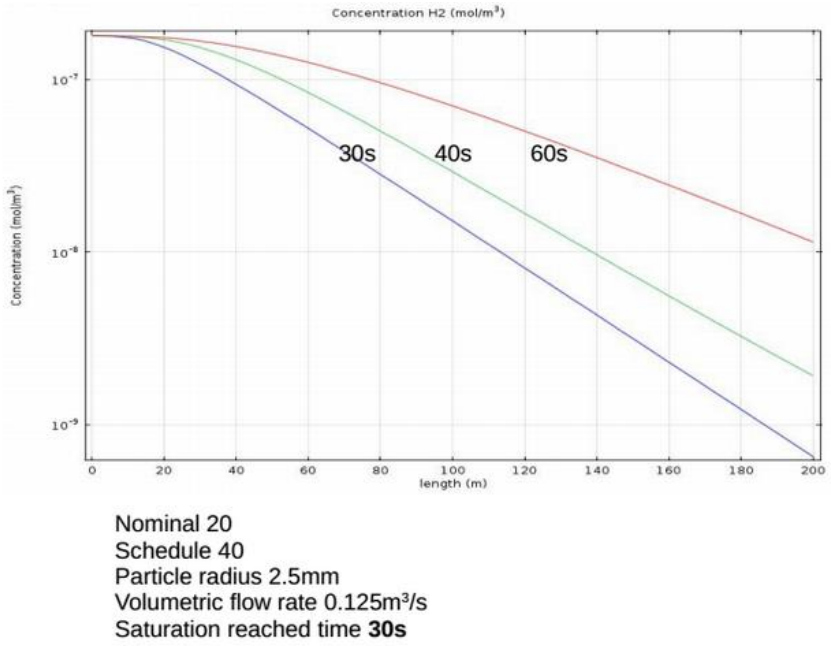

Figure 2.2 H_2 concentration distribution of model D20S40c (see Table 2.1)

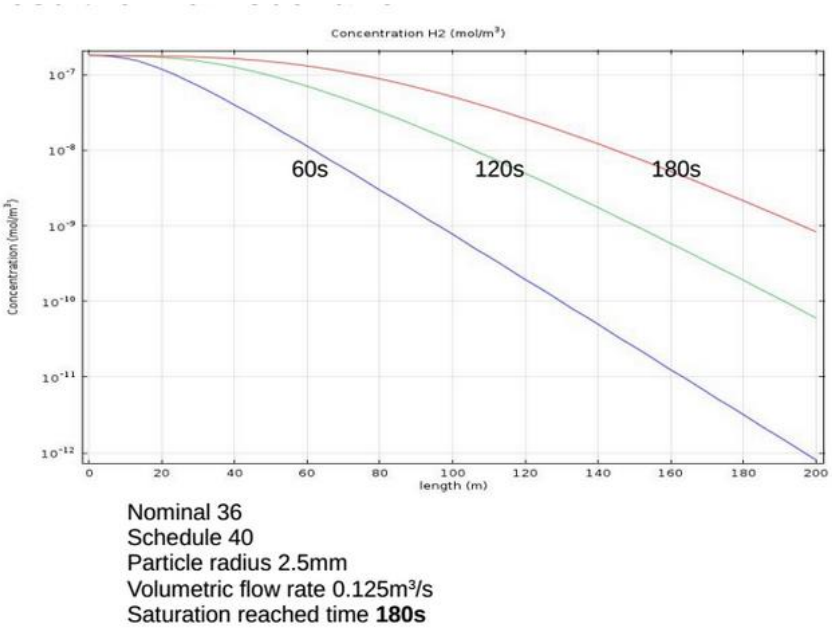

Figure 2.3 H_2 concentration distribution of model D36S40b (see Table 2.1)

Table 2.1 also shows a summary of simulation results for the stainless steel packed bed design. The AHTR pre-conceptual design [3] is used for evaluation of the tritium removal efficiency of the design. In this simulation, two sets of commercial pipe sizes (nominal pipe size 20 in, Schedule 40 and nominal pipe size 36 in, Schedule 40) are used. A_{ratio} is the ratio of the pipe inner diameter to the stainless steel ball diameter, which is called the aspect ratio. ε is the porosity, defined as the volume fraction that is not taken by the stainless steel balls. The stainless steel balls were assumed to have a slightly looser packing pattern compared to the densest packing (ε=26%). Therefore, ε was set at 40% in the calculations. By checking the dimensions of the proposed facility needed to fulfill the cleanup task of the molten salt flow rate proposed in the AHTR pre-conceptual design, the total length needed is estimated as listed in the right most column of Table 2.1.

Comparing the different models in Table 2.1, it can be seen that for a cylinder packed bed with a 34.5 in (0.876 m) inner diameter and 200 m length, it takes about 3 minutes for 0.0098-in (2.5-mm) radius stainless steel balls to reach the tritium saturation limit. There are two ways to delay the stainless steel balls reaching saturation. The first is to increase the facility cross-sectional area. Since the volumetric flow rate of the molten salt is constant, the flow velocity will decrease accordingly by increasing the salt flow area. As a result, it takes the stainless steel balls longer time to become tritium saturated. The second is to increase the facility length. To achieve this, the pipes can be bended or coiled to reduce the length or height of the facility.

This exercise again shows that obtaining a large mass transfer surface area to volume ratio is the key for the tritium removal facility design.

2.3 Finned plate tritium removal facility design

Our literature review and previous calculations have demonstrated the necessity of a high surface area to volume ratio for the design of the tritium removal facility. Since the problem is similar to heat

transfer problems, the methods used to increase surface area in heat exchanger design can be adopted. The method used in this design is to add fins in the molten salt flow path.

Figure 2.4 shows the cross sectional view of two flow passages in the facility. The design of the facility is based on the idea of a plate-type compact heat exchanger. The structure material is stainless steel 316. The molten salt flows inside the finned semi-circular channel, while the purging gas flows inside the open semi-circular channel. The diameters of both flow channels are 2 mm, and the horizontal pitch of the channels on the same plate is 3 mm. The plate thickness is set to be 80% of the channel diameter [17], namely, 1.6 mm as shown in Figure 2.4. The fins in the molten salt channels are straight fins made of stainless steel 316. Five fins are arranged radially and uniformly in each channel, with 0.66 mm in height, and 0.1 mm in thickness. In this design, the mass transfer area per unit volume in the molten salt reaches 738 m^2/m^3.

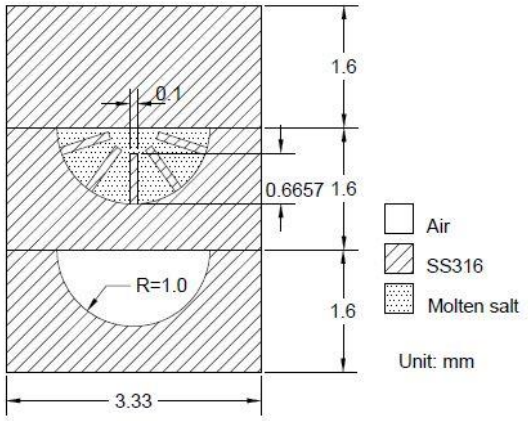

Figure 2.4 Cross-sectional view of the finned plate tritium removal facility model (unit cell)

FLiNaK and air are used as the materials for the molten salt and the purging gas respectively. Similar to previous designs, air will be heated before entering the facility. Air could be a candidate of purging gas, as long as the tritium concentration at the outlet of the facility does not reach the explosion limit and the oxygen does not cause corrosion concerns. The velocity of the molten salt is set as 0.1 m/s, while that of the purging gas is 0.5 m/s. Both flows are in the laminar flow regime. As in the model described in Section 3.3, the stiff-spring boundary condition is used at the interfaces of the two adjacent diffusion domains.

A computer simulation was performed using COMSOL Multiphysics, and the results are shown in Figure 2.5 and Figure 2.6. In Figure 2.5, the H_2 concentration distribution at steady state along the probe shown in the right schematic is plotted. The *x*-axis is the distance along the probe line in the unit of meter. The *y*-axis is the H_2 concentration in the unit of mol/m^3, In this simulation, the initial H_2 concentration in the molten salt is again 1.8×10^{-7} mol/m^3. In Figure 2.6, cut views at different positions of H_2 concentration are shown to help understand the H_2 diffusion process in the molten salt flow direction. As can be seen from the figures, the H_2 concentration gradient is mainly in the molten salt domain. Since the flow is laminar, not much mixing happens in the flow. Therefore, the H_2 concentration gradient in the molten salt prohibits the H_2 from being extracted. Another concept must be used which mixes the molten salt in very small channels.

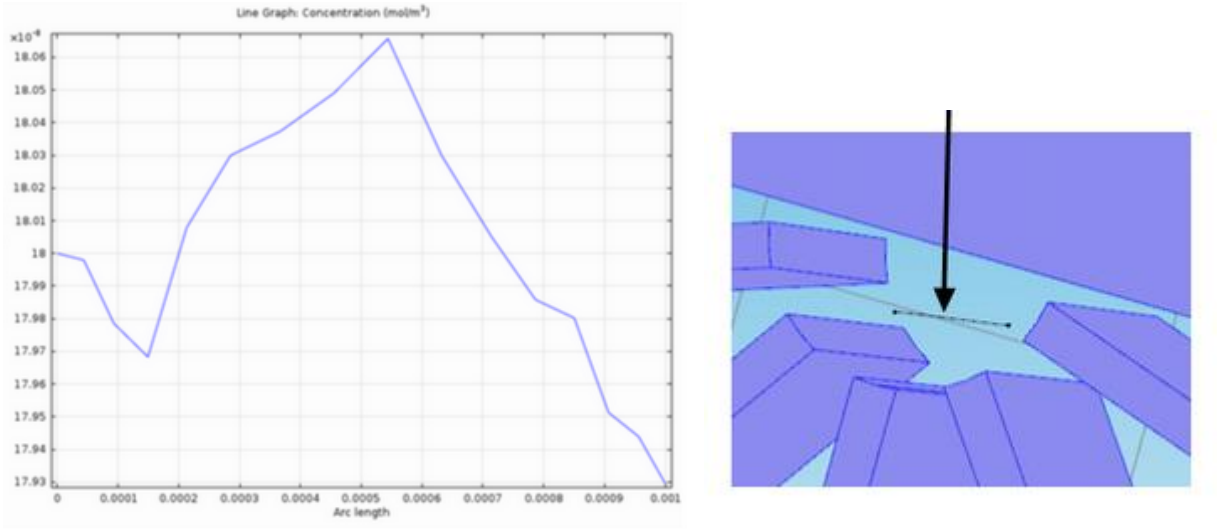

Figure 2.5 H_2 concentration distribution along probe line in the molten salt channel

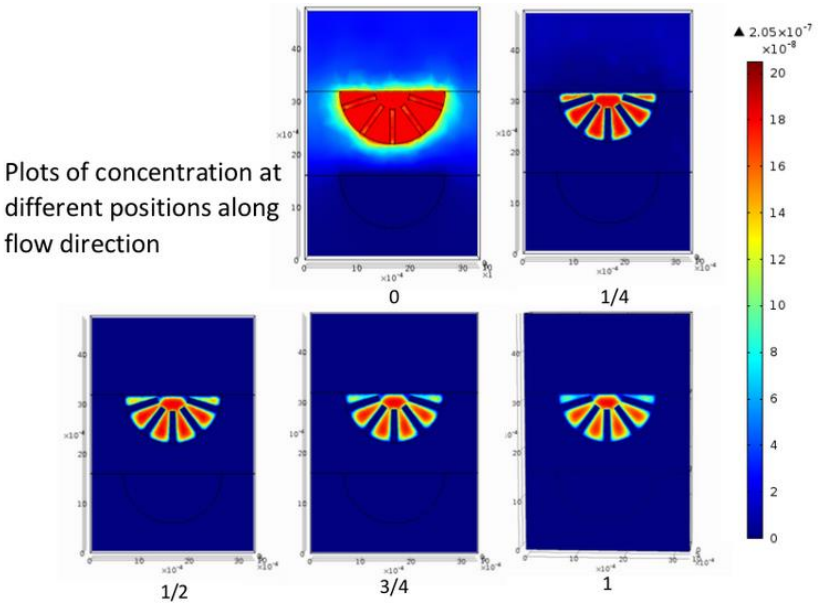

Figure 2.6 Cross-sectional views of the H_2 concentration distribution along the flow direction

2.4 Wavy-plate tritium removal facility design

To enhance the molten salt mixing and transport of the tritium in the salt, a design with wavy plates was proposed. Similar to the finned plate design, this design uses a plate-type compact heat exchanger as its original model. Figure 2.7 shows the cross sectional view of the facility. There are five layers in total in Figure 2.7: from the top to bottom, the second and forth layer are the base structural plates made of stainless steel 316. On the top and bottom of these two plates are the path for the purging gas, and the molten salt flows in the channel between the two stainless steel plates.

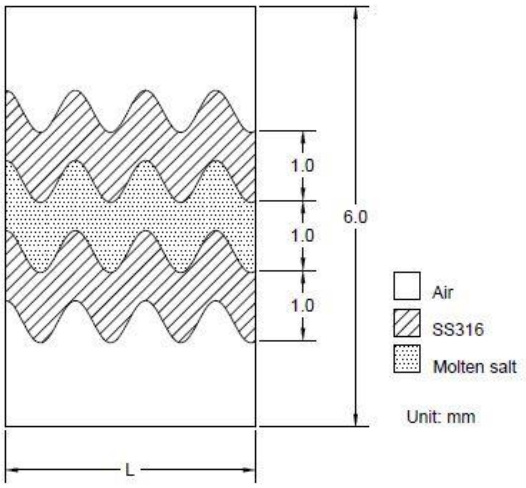

Figure 2.7 Cross-sectional view of 2-D wavy plate design (unit cell)

The thickness of the stainless steel plates is 1.0 mm, which is the same as the height of the molten salt flow passages. For simplicity, the curvature of the plates in the simulation is expressed by a sine function:

$$y = 0.3\sin\left(\pi x^2 + \frac{\pi}{2}\right) \tag{10}$$

where, x and y are the positions in height and length directions, respectively. In the simulation, FLiNaK and air are used as the materials for the molten salt and the purging gas respectively. The molten salt flow velocity is set as 0.1 m/s while the air flow velocity is 0.5 m/s in the same direction as the molten salt. Both flows are laminar flow. As to the H_2 diffusion settings, no flux boundary condition is assigned to the top and bottom boundaries, and the stiff-spring boundary condition is assigned at the interfaces of the adjacent diffusion domains.

A 2-D simulation was carried out using COMSOL Multiphysics and the results are shown in Figure 2.8, Figure 2.9 and Table 2.2. Considering the efficiency of computer simulation, we set the simulation length (in the x-direction) of the model to be 100 mm. Same as in the above mentioned simulations, the inlet H_2 concentration was set at the same level as the average T_2 production rate suggested in the AHTR pre-conceptual design, which was 1.8×10^{-7} mol/m^3 [3]. After the outlet H_2 concentration at the centerline of the molten salt flow reached a steady state, it was used as the inlet H_2 concentration for the next calculation. This calculation process was repeated for five times, as shown in Table 2.2. In this way, the H_2 diffusion behavior in a long geometry can be approximately modeled using a shortened geometry.

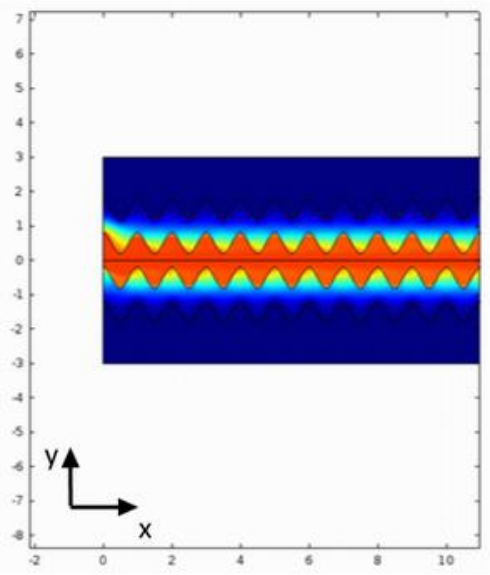

Figure 2.8 H_2 concentration distribution in a wavy-plate tritium removal facility

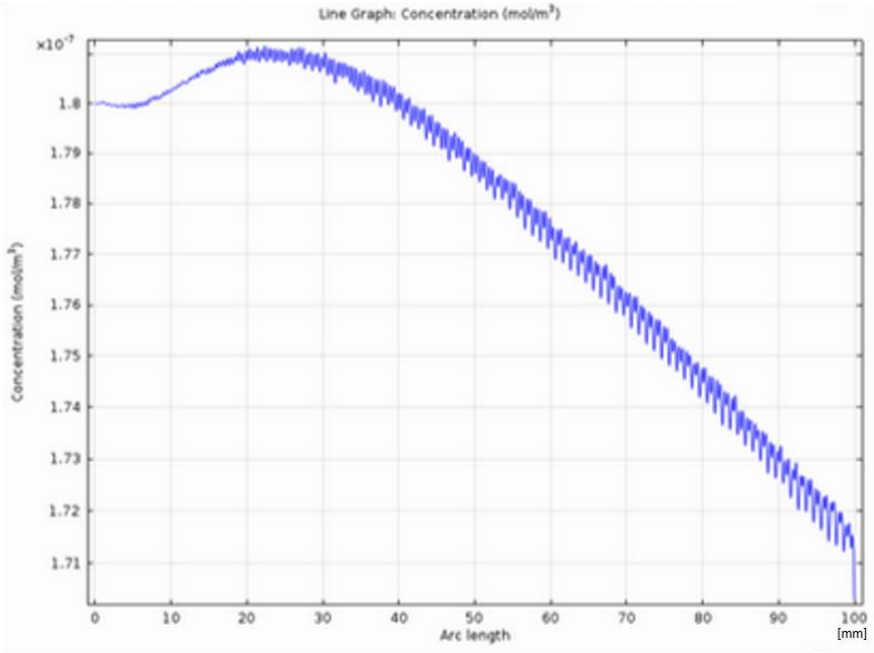

Figure 2.9 H_2 concentration along the center line of molten salt flow in a wavy-plate tritium removal facility

Table 2.2 Results of the wavy-plate tritium removal model

	H_2 inlet concentration [$\times 10^{-7}$ mol/m^3]	H_2 outlet concentration [$\times 10^{-7}$ mol/m^3]	$\|\Delta\|$
1	1.8	1.71	0.09
2	1.71	1.625	0.085
3	1.625	1.54	0.085
4	1.54	1.46	0.08
5	1.46	1.385	0.075
...	…	…	…
Last		0.09 (95% H_2 removal)	

Figure 2.8 shows the distribution of the computed steady-state H_2 concentration by the model. The red color represents a high concentration of H_2 and blue represents a low H_2 concentration. The basic pattern shown in Figure 2.8 can be applied to any position along the flow direction. The H_2 concentration distribution in the stainless steel plate is high near the molten salt, but decreases quickly towards the air side. The maximum H_2 concentration in the molten salt shows a wavy curve in accordance with the shape of the stainless steel plates. In the stainless steel domain, near the surface which encounters the molten salt flow, the H_2 concentration is obviously higher than that near the surface on the other side.

In Figure 2.9, the centerline H_2 concentration distribution from the inlet to a location 100 mm downstream was plotted. The peak appearing at about 20 mm away from the inlet might be due to the mixing and development of the molten salt flow. A 0.5% decrease in H_2 concentration was observed after 100 mm. From the results listed in Table 2.2, a decrease in H_2 concentration can be observed after each calculation. The amount of decrease shows a decreasing trend as the number of calculation increases, because as the flow path becomes longer, the concentration difference between the molten salt and the stainless steel plate will decrease. This decreasing concentration difference gives a lower mass transfer flux. However, 0.04 mol/m^3 can be assumed as the lower limit of the H_2 concentration decrease during each calculation, till the outlet H_2 concentration reaches 0.09 mol/m^3, which is the goal for 95% tritium removal. Under this assumption, the total flow length needed is 4.3 m, which appears acceptable for a tritium removal facility.

This distribution of the H_2 concentration leads to the conclusion that enhancing the mixing of the molten salt flow is a method to increase the tritium removal efficiency.

2.5 Cross-flow tritium removal facility design

The results of the wavy-plate flow path design suggest that it is reasonable to develop a design that can promote the molten salt flow mixing. Again from the heat exchanger design, the concept of a cross-flow tritium removal facility is proposed. Figure 2.10 shows the molten salt flow streamlines in this design. The purging gas will flow inside the tubes while the molten salt will be in a cross-flow setting to the tubes, as shown in the figure. The tubes are staggered so that the salt stream containing the maximum H_2 concentration possible will fully contact with a tube and flow around the tube. In this way, not only the maximum H_2 concentration difference can be assured at the mass transfer interface,

but also the molten salt flow will be well mixed. Based on this design concept, a cross-flow tritium removal facility is proposed and designed. The details are discussed in the following sections.

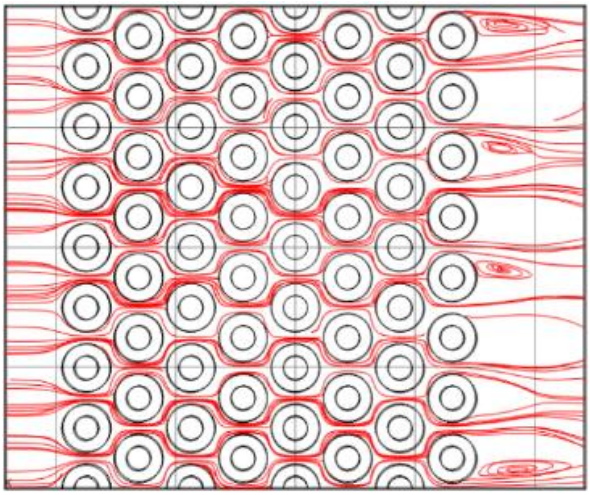

Figure 2.10 Flow stream line of the molten salt in the cross-flow tritium removal facility design

Table 2.3 summarizes the modeled design concepts for the tritium removal facility. The results from computational simulations are compared. The mass flow rate of the molten salt in each case has a constant value of 1 kg/s. The total flow length of the molten salt needed to achieve a 95% H_2 removal is obtained from the computer simulation.

Table 2.3 Comparison of the five design concepts for tritium removal facility

Design concept	Mass transfer surface area per unit volume [m^2/m^3]	Molten salt inlet flow area [m^2]	Molten salt flow velocity at the inlet [m/s]	Total molten salt flow length needed [m]*	Advantages	Disadvantages
Helium gas purging method (1 mm bubble diameter, ε=90%)	600	27.7	0.2	200	Post processing does not require complicated methods.	To keep a high enough bubble volume fraction is not feasible
Stainless steel packed bed scrubber (D20S40a)	354	0.79	6.975	2200	The packed bed facility design is mature.	Low efficiency of tritium removal requires a large facility
Finned-plate design	738	55.4	0.1	>3000	The finned heat exchanger design is mature.	Low efficiency of tritium removal requires a large facility
Wavy-plate design	711	55.4	0.1	38	Relatively high tritium removal efficiency.	Dimensions of the facility are large
Cross-flow design	1005	55.4	0.1	27	Relatively high tritium removal efficiency.	High molten salt pressure drop requires large pumping power

*Based on a 95% H_2 removal of the 1.8×10^{-7} mol/m^3 initial tritium concentration in the molten salt.

2.6 Cross-flow tritium removal facility

From the comparison of the five tritium removal facility designs, it is clear that the cross-flow design gives the most promising results. Detailed dimensions and material selections were then determined based on literature review and computer modeling.

2.6.1 Sweep gas selection

Table 2.4 shows the diffusion coefficients of tritium in several candidate purging gases. Tritium diffusion coefficients in nitrogen, air and carbon dioxide are on the same order of magnitude (10^{-4} m^2/s), while that in helium is one order of magnitude higher (10^{-3} m^2/s). However, tritium transport coefficients in gases are several orders of magnitude higher than those in the molten salts (FLiBe and FLiNaK, to be more specific) or in the wall structural materials. Therefore, the mass transport resistance in the sweep gas is negligible in the overall mass transport resistance. One major concern in the gas selection is its radioactive stability under high neutron flux conditions. Helium is a good candidate in that regard.

Table 2.4 Tritium diffusion coefficients in different gases

Gas	Correlation D in [m^2/s], p in [atm]	Temperature [K]	Diffusion coefficient [$\times 10^{-4}$ m^2/s]	References
He	$D = 1.032 \times 10^{-8} T^{1.74}$	977	16.4	[18]
			11.27	[19]
N_2	$D = \frac{1.539 \times 10\text{-}6 T 1.548}{\ln\left(\frac{T}{3.16 \times 107}\right) 2 \exp\left(\frac{1067}{T2} - \frac{2.8}{T}\right)} p$ $D = \frac{1.539 \times 10^{-6} T^{1.548}}{\ln\left(\frac{T}{3.16 \times 10^{7}}\right)^{2} \exp\left(\frac{1067}{T^2} - \frac{2.8}{T}\right) p}$		6.08	[20]
			5.548	[19]
Air	$D = 3.64 \times 10^{-9} T^{1.75} p$		6.21	[20]
			5.639	[19]
CO_2	$D = \frac{3.14 \times 10^{-5} T^{1.75}}{\exp\left(\frac{11.7}{T}\right)} p$		5.3	[20]
			4.720	[19]

2.6.2 Mass transfer compared with heat transfer

Mass transport processes show a great similarity with heat transfer processes. Counterpart heat and mass transfer parameters are listed in Table 2.5 [21]. Table 2.6 shows the distribution of resistance for tritium diffusion from the primary coolant (molten salt) into the sweep gas (air). The geometry for this calculation is listed in Table 2.7. From Table 2.6 it can be seen that the largest mass transport resistance is in the molten salt. The next major resistance is in the tube wall. The tritium diffusion rate in the sweep gas is six orders of magnitude greater than that in the molten salt and three orders of magnitude greater than that in the tube wall. As predicted, the resistance due to tritium diffusion in the purging gas is negligible. The key issues to increase the tritium removal performance of the facility is to improve the tritium diffusion rates in the molten salt and tube wall.

Table 2.5 Mass transfer parameters

No.	Mass transfer	Heat transfer
1	Reynolds number $\mathrm{Re} = \frac{\rho v D_h}{\mu}$	Reynolds number $\mathrm{Re} = \frac{\rho v D_h}{\mu}$
2	Schmidt number $\mathrm{Sc} = \frac{\mu}{\rho D_{AB}}$	Prandtl number $\mathrm{Pr} = \frac{c_p \mu}{k} = \frac{\nu}{\alpha}$
3	Sherwood number $Sh = \frac{k_x D_h}{D_{AB}}$, etc	Nusselt number $\mathrm{Nu} = \frac{h D_h}{k}$
4	Peclet number $\mathrm{Pe} = \mathrm{Re}\,\mathrm{Sc}$	Peclet number $\mathrm{Pe} = \mathrm{Re}\,\mathrm{Sc}$
5	Grashof number $\mathrm{Gr} = \frac{gL^3(\Delta\rho)}{\rho}\left(\frac{\rho}{\mu}\right)^2$	Grashof number $\mathrm{Gr} = \frac{g{D_h}^3\rho^2\beta(\Delta T)}{\mu^2}$ β=thermal expansion coefficient
6	Stanton number $\mathrm{St} = \frac{\mathrm{Sh}}{\mathrm{Re}\,\mathrm{Sc}} = \frac{\mathrm{Sh}}{\mathrm{Pe}}$	Stanton number $\mathrm{St} = \frac{\mathrm{Nu}}{\mathrm{Re}\,\mathrm{Pr}} = \frac{\mathrm{Sh}}{\mathrm{Pe}}$

Table 2.6 Mass transport parameters (with comparison to heat transfer parameters)

	Mass transfer	Heat transfer	Molten salt	Air	Stainless steel tube wall
1	Velocity [m/s]	Velocity [m/s]	0.1	1	
2	Re	Re	692.86	17.2	
3	$\mathrm{Sc} = \frac{\mu}{\rho D_{AB}}$ Schmidt number	Pr	546.7	1.941	
4	$\mathrm{Sh} = \frac{Fl}{cD_{AB}}$ Sherwood number	Nu	135.96	5.1	
5	$k = \frac{F}{c}$ mass transfer coefficient [m/s]	h heat transfer coefficient	3.88×10^{-11}	0.00588	1.5×10^{-8}

$*l$ is unit length, or the diameter of a circular tube

Table 2.7 Geometry for mass transfer resistance calculation

Tube outer diameter [mm]	4
Tube inner diameter [mm]	2
Tube bank pitch [mm]	5
Tube bank arrangement	Staggered

2.6.3 Determination of geometric parameters

It is expected that via adjustments of the geometric parameters, optimized dimensions of the tritium removal facility can be determined. Therefore, calculations were performed with different tube bank pitches, tube inner diameters, tube wall thicknesses, and fluid flow rates. Changes in the tritium concentration and pressure drop due to the molten salt flow across the unit cell were recorded.
The pressure drop of the molten salt through the entire facility is affected by the total length needed to achieve the desired tritium removal. There are two ways to determine the length. One is to divide the desired amount of tritium removed by the decrease of tritium concentration obtained from the COMSOL model simulation Δc_{unit} and then multiply that obtained value by the length of the model l_{unit}:

$$L_{mt} = \frac{99\% c_0}{\Delta c_{unit}} l_{unit} \tag{11}$$

The second method is to use correlations in Table 2.5 to calculate the total length needed for a desired amount of tritium removal.

Similarly, for the calculation of the pressure drop, there are also two methods. One is to obtain the pressure drop for the unit model from the COMSOL simulation and then scale the result up for the total length obtained from the COMSOL simulation for the unit cell. The other is to use fluid flow correlations and calculate the pressure drop according to the geometry and total flow length determined above. However, the total length can be either the one obtained from the COMSOL simulation, i.e., from Equation (11) or calculated from the mass transfer correlations.

Taking all the above methods into account, for calculation of the pressure drop of the molten salt through the entire facility, there are three methods that can be used:

1. COMSOL: Using the tritium concentration decrease for a unit cell obtained from the COMSOL Multiphysics results, the total number of the unit cells required to get the 95% tritium removal efficiency can be identified. The total pressure drop is obtained by multiplying the computed molten salt pressure drop of a unit cell by the number of cells needed.
2. MATLAB A: A MATLAB code (Code A) was written to calculate the molten salt pressure drop using standard fluid flow correlations. The total length used in this MATLAB model was obtained from the COMSOL Multiphysics unit cell model.
3. MATLAB B: Another MATLAB code (Code B) was also written based on the mass transfer correlations. This code calculates the total length of the tritium removal facility with correlations shown in Table 2.5. Then this total length of the facility was fed to Code A to obtain the molten salt pressure drop.

A set of bare tube banks of reasonable dimensions were calculated using the above described methods. With COMSOL Multiphysics, a three dimensional (3-D) model of the cross-flow tritium removal facility unit was built, as shown in Figure 2.11. In this unit model, only nine tubes are included. Stainless steel plates are placed on both the top and bottom sides of the molten salt channel. Molten salt flows into the unit from Face 1 and flows out of the unit from Face 2. For Faces 3 and 4 on the sides of the unit, symmetrical boundary conditions are applied. Air is used as the purging gas, flowing into the tube bank from the bottom side and exiting from the top. It is assumed no tritium leakage from the edges of the steel plates or tubes. All the tritium that enters the unit with the molten salt will either exit with the molten salt from Face 2 or diffuse into the purging gas through tube walls and leave the unit with the purging gas. The total height of the unit model is 4 mm. Both stainless steel plates are 0.3 mm in thickness. The total length of the molten salt channel is ten times the outer diameter of the tubes. For simplification, the name "Tritium Removal Unit Model" is used in this report to refer to this model.

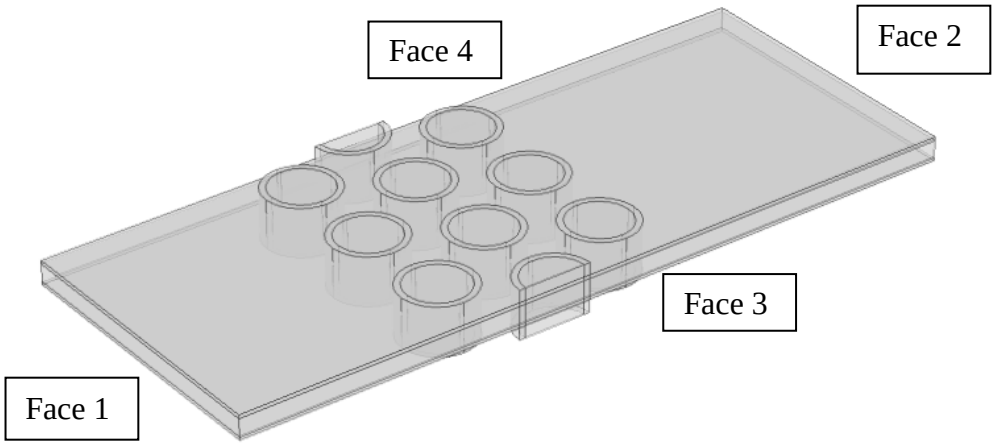

Figure 2.11 Unit model for the cross-flow tritium removal facility (Tritium Removal Unit Model)

Note that in this unit model for simulation, the inflow and outflow regions for the molten salt are much longer than an actual unit will have. Also, the tube bank extends beyond the top and bottom of the molten salt channel to eliminate the influence of boundary conditions from adjacent domains, and to ensure fully-developed flow of molten salt before flowing into the tube bank. The unit cell used for subsequent calculations includes only the portion which houses the tube bank, i.e., without the entrance and exit regions on the salt side. Comparing the obtained results for various dimension and flow condition combinations shown in Table 2.9, #18 has the best performance, with main considerations on the molten salt pressure drop and tritium removal efficiency. The dimensions and flow conditions used in #18 are listed in Table 2.8. The results are also plotted in Figure 2.12.

Table 2.8 Dimensions of Tritium Removal Unit Model

Tube inner diameter [mm]	5	Tube wall thickness [mm]	0.5
Tube outer diameter [mm]	6	Molten salt flowing velocity [m/s]	0.05
Tube bank pitch [mm]	8	Air flowing velocity [m/s]	0.5

Table 2.9 Pressure drop of molten salt flowing across a tube bank

Model number #	Pitch [mm]	Tube outer diameter [mm]	Tube inner diameter [mm]	Tube wall thickness [mm]	Molten salt flow velocity [m/s]	Molten salt outlet tritium concentration [$\times 10^{-8}$ mol/m^3]	Decrease of tritium concentration in molten salt after a unit cell [$\times 10^{-11}$ mol/m^3]	Total length of facility by COMSOL [m]	Frontal area of facility [m^2]	Frontal area diameter [m]	Total volume of facility [m^3]	Molten salt total pressure drop by COMSOL [$\times 10^5$ Pa]	Molten salt pressure drop by Matlab A [$\times 10^5$ Pa]	Total facility length by Matlab B [m]	Molten salt pressure drop by Matlab B [$\times 10^5$ Pa]
1	7	4	2	1	0.1	5.81	1.48	243	55	4	13442	39.6	16.5	242	104
2	5	4	2	1	0.1	5.81	2.66	96	55	4	5342	71.7	12	781	97
3	5	3	1	1	0.05	5.81	1.90	135	111	6	14958	12.1	3.8	623	17.5
4	8	4	2	1	0.05	5.81	1.86	221	111	6	24447	10.8	3.35	1011	15.3
5	6	4	2	1	0.05	5.81	2.71	114	111	6	12585	12.0	2.5	566.6	12.4
6	5	4	2	1	0.05	5.81	3.93	65	111	6	7232	18.0	2.3	392	13.8
7	6	5	3	1	0.05	5.81	4.79	64	111	6	7120	20.3	2.21	416	14.4
8	7	5	3	1	0.05	5.81	3.39	106	111	6	11737	12.7	1.98	568	10.6
9	6.5	5	3	1	0.05	5.81	3.94	85	111	6	9377	14.7	1.94	489	11.2
10	8	6	4	1	0.05	5.81	4.08	101	111	6	11145	13.5	1.71	416	9.97
11	6	3	2	0.5	0.05	5.81	3.84	80	111	6	8881	4.45	1.7	338	7.2
12	5	4	2	1	0.025	5.80	5.78	44	222	8	9834	4.91	1.65	197	1.96
13	5	3	2	0.5	0.05	5.81	5.00	51	111	6	5684	4.58	1.44	634	6.58
14	8	4	3	0.5	0.05	5.81	4.35	94	111	6	10453	4.64	1.42	428	6.48
15	10	7	5.5	0.75	0.05	5.80	5.31	97	111	6	10704	9.05	1.17	551	6.68
16	7	3	2	0.5	0.1	5.81	2.14	168	55	4	9296	16.5	1.09	911	5.91
17	6	4	3	0.5	0.05	5.80	6.37	48	111	6	5354	5.10	1.05	239	5.236
18	8	6	5	0.5	0.05	5.80	8.95	46	111	6	5081	6.17	0.779	268	4.54
19	10	7	6	0.5	0.05	5.80	8.12	63	111	6	7000	5.92	0.753	356	4.31
20	7	3	1	1	0.05	5.81	1.29	278	111	6	30844	11.3	0.51	1225	2.25
21	6	4	2	1	0.025	5.81	4.23	73	222	8	16125	3.23	0.454	330	1.77
22	7	3	2	0.5	0.05	5.81	3.35	107	111	6	11877	4.34	0.197	462	0.85
23	7	3	1	1	0.025	5.81	2.10	171	222	8	37894	3.09	0.089055	618	0.322

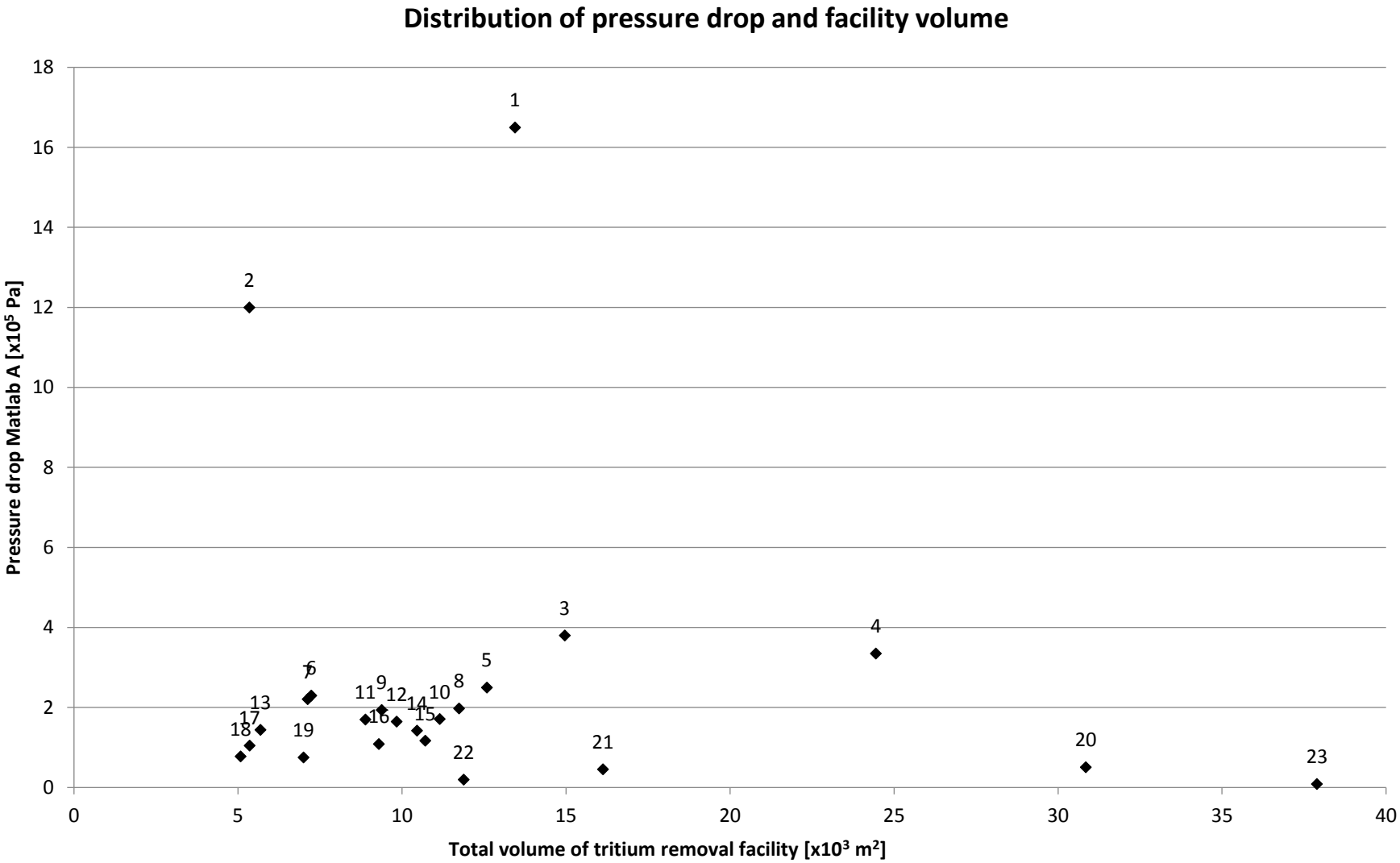

Figure 2.12 Pressure drop and facility volume for different design points of the Tritium Removal Unit Model

2.6.4 Determination of fluid flow rates

Calculations have been performed to compare the mass transport resistances of the tritium removal facility with various fluid flow rates. It is assumed in the current study that the velocity of the sweep gas does not have a significant impact on the overall tritium removal performance. This assumption is made from the observation of the simulation results that tritium removal efficiency does not change notably when the purging gas velocity changes between 0.1 m/s and 40 m/s. This is due to the low mass transport resistance of the purging gas. The influence of molten salt velocity on the overall mass transport coefficient is shown in Table 2.10 and Figure 2.13. The overall mass transfer coefficients are calculated using Code B at different molten salt velocities. The increase of overall mass transport coefficient becomes smaller with increasing molten salt velocity at higher salt velocities. As molten salt velocity increases from 0.03 m/s to 0.05 m/s, the overall mass transport coefficient increases by 2.22%. However, from 0.05 m/s to 0.1 m/s, the overall mass transport coefficient increases by only 1.92%. And from 0.5 m/s to 1 m/s, the increase is 0.31%.

Table 2.10 Impact of molten salt velocity on overall mass transfer coefficient

Molten salt velocity [m/s]	Overall mass transport coefficient [$\times 10^{-6}$ m^3/s]	Percentage increase [%]
0.01	0.980	
0.02	1.044	6.49
0.03	1.070	2.49
0.04	1.084	1.36
0.05	1.094	0.86
0.1	1.115	1.92
0.2	1.127	1.11
0.3	1.132	0.42
0.5	1.136	0.36
0.8	1.138	0.23
1	1.139	0.079

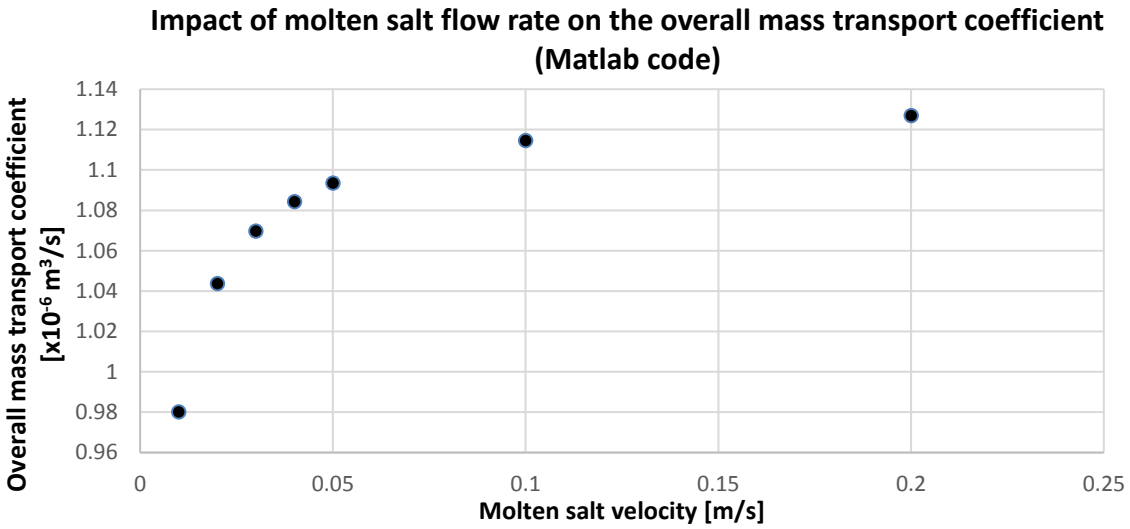

Figure 2.13 Impact of molten salt velocity on overall mass transfer coefficient

These results were used to determine the fluid velocities. With the increase of molten salt flow velocity, mass transport performance becomes better. However, when the velocity is larger than 0.05 m/s, an increase is velocity does not yield a corresponding increase in efficiency. Therefore, 0.05 m/s is a suitable molten salt flow velocity.

2.6.5 Elevated tritium concentration level in the primary loop

From the mass transport theory, concentration difference is the driving force of mass transfer. Therefore, to make tritium extraction more efficient, an elevated tritium concentration in the primary coolant was proposed. The impact of higher tritium concentration level in the molten salt on the length of tritium removal facility was simulated with the Tritium Removal Unit Model. Figure 2.14 shows the simulation results. c_0 is the tritium production rate of a FHR under steady state operation, which is 1.8×10^{-7} mol/m^3 [3].

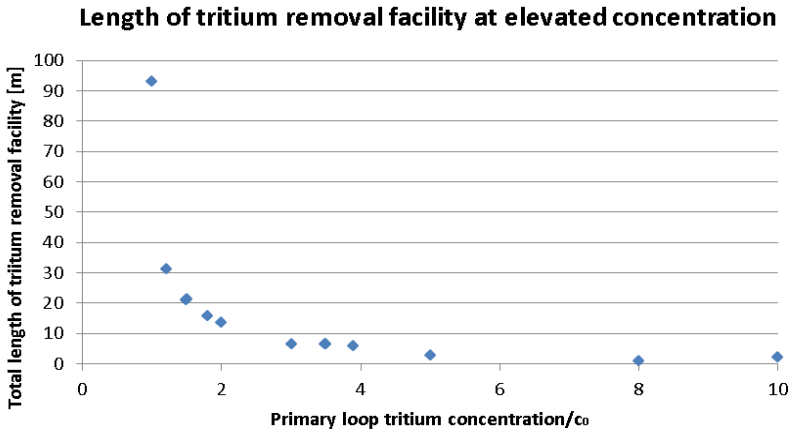

Figure 2.14 Length of tritium removal facility at elevated tritium concentration in primary loop

As the tritium concentration in the primary loop firstly starts to increase, the total length of the facility needed decreases very quickly. However, after the initial tritium concentration reaches three times of the production rate c_0, the decrease in total length slows down. If the initial tritium concentration is five times of c_0, the total length is about 5 m, according to the simulation results. In this situation, the dimension of the tritium removal facility is reasonable in terms of construction and operation.

2.6.6 Design of the cross-flow tritium removal facility

The finalized cross-flow tritium removal facility is shown in Figure 2.15. In this drawing, only a quarter of the whole tube bank is presented in the front right conner, while in the real facility the tube bank is occupy the entire space of the facility. It is designed with modular concept in mind, in order to meet different demands in FHRs of different power levels. Multiple modules can be bolted togeter in a row, increasing the total avtive length of tritium removal area, or they can be bolted side by side to a main pipe, spliting the molten salt flow, as shown in Figure 2.16.

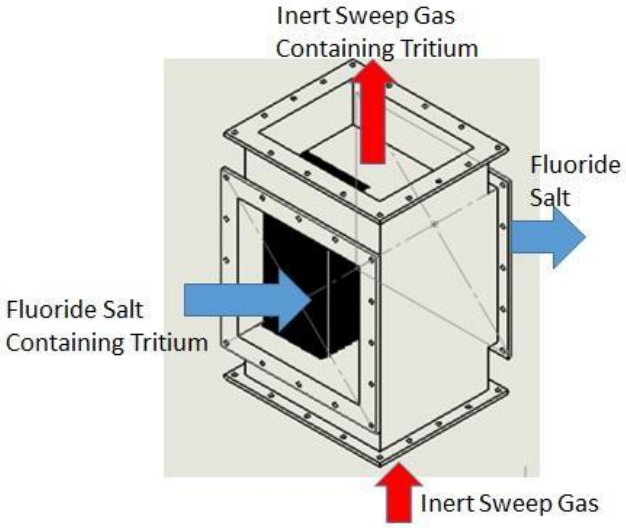

Figure 2.15 Cross-flow tritium removal facility

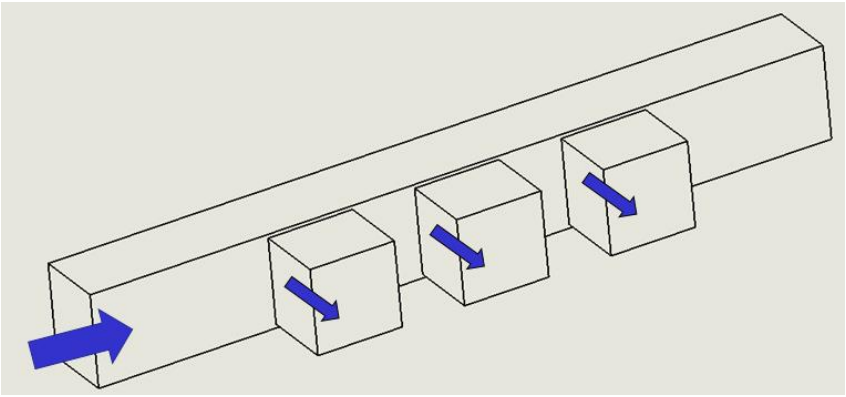

Figure 2.16 Tritium removal modular facilities connected to a main pipe

For the detailed dimensions, two cases where the best results in both mass transfer performance and pressure drop among total twenty five models that have been simulated were selected, as listed in Table 2.11. The total mass flow rate of the molten salt and the tritium inlet concentration are from the pre-conceptual design of the Advanced High Temperature Reactor (AHTR) [3].

Table 2.11 Configurations of the tritium removal facility

Items	Unit	Design A	Design B
Total mass flow rate of molten salt	kg/s	11190.8	
Tritium concentration in inlet molten salt	mol/m^3	1.8×10^{-6}	
Tritium concentration in outlet molten salt	mol/m^3	1.62×10^{-6}	
Objective tritium removal rate	mol/s	1.02×10^{-6}	
Tube outer diameter	mm	26.67	33.40
Tube inner diameter	mm	20.93	26.64
Tube wall thickness	mm	2.87	3.38
Tube bank pitch	mm	33.27	41.66
Number of tubes	–	729	441
Molten salt inlet frontal velocity	m/s	1	1
Number of modules required	–	24	36

In the finalized designs, the tritium concentration in the primary coolant is intentionally raised to 10 times of its production rate (1.8×10^{-7} mol/m^3-s). As a result, the tritium concentration difference between the primary coolant and the purging gas is raised, which leads to a larger mass transfer driving force. Therefore, the designed cross-flow tritium removal facility characterizes: a large ratio of mass transfer area over volume, a highly turbulent molten salt flow, and a large gradient of the tritium concentration.

2.7 Validation experiment of the tritium removal facility with molten salt surrogate

Experiments were designed for the validation of the effectiveness of the tritium removal facility. For safety concerns, hydrogen is used as a surrogate for tritium. Before formally performing experiments using molten salt, testing experiments were planned using surrogates for the molten salt. Due to time constraint and delay in the construction of the equipment in the lab, the experiments have not been completed by the date that the final report is written. In the future, if permitted, both experiment will be carried out.

2.7.1 Surrogate for molten salt

The surrogate selected is better to have large enough hydrogen solubility, be physically and chemically stable, not be corrosive to structure materials and have viscosity close to the molten salt. In addition, it would be advantageous if the testing experiments can be conducted at room temperature. But the high

hydrogen solubility is the most important criterion for the selection of potential surrogates since it is the key factor to determine whether or not the hydrogen in the samples collected can be detectable. Water as the most common solute is studied first. Hydrogen solubility in water has been investigated by several research groups. Gevantman took the values of hydrogen solubility in water listed in the International Union of Pure and Applied Chemistry "Solubility Data Series" and fitted them into a correlation [22]:

$$\ln S = -48.1611 + \frac{55.2845}{\frac{T}{100}} + 16.8893 \ln \frac{T}{100} \tag{12}$$

where the applicable temperature range is 273.15 to 353.15 K, and the unit of solubility is mole fraction of hydrogen to water.

Hydrogen solubility in water is also plotted in Figure 2.17 [23]. The temperature range of this plot is 0 to 60 degree Celsius. And solubility is expressed in the unit of weight fraction of hydrogen to water.

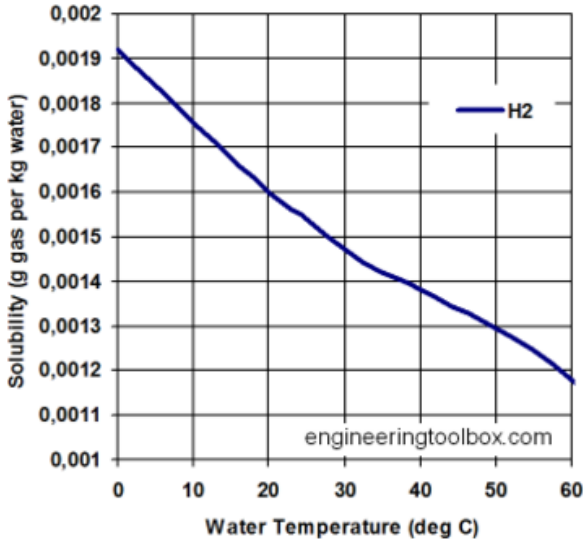

Figure 2.17. Hydrogen solubility in water [23]

A simple comparison of H_2 solubility in water obtained from the above mentioned models [22][23] is shown in Figure 2.18 and Table 2.12. From the figure it can be observed that H_2 solubility in water is consistent across different models. The relative error shown in the table also confirms the consistence of H_2 solubility in water.

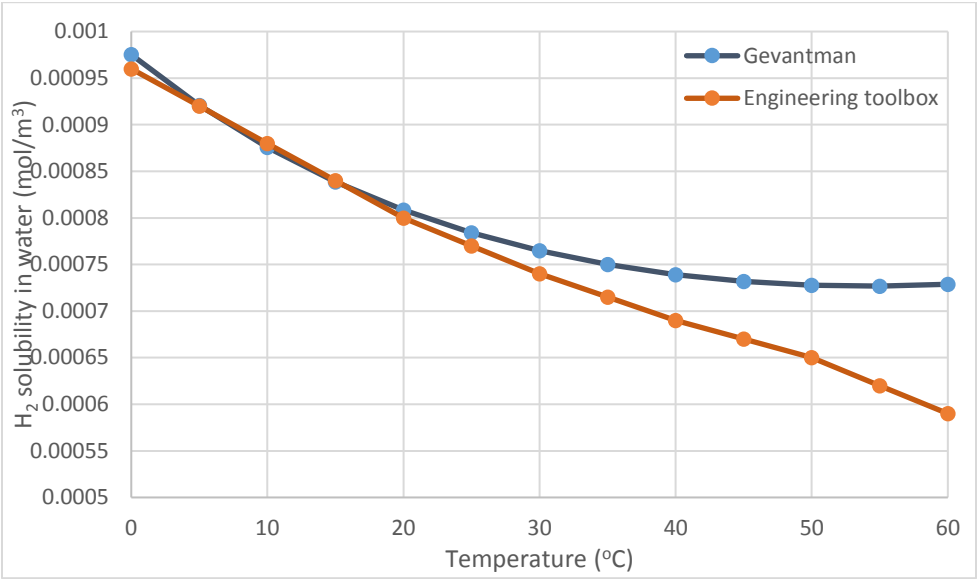

Figure 2.18. Comparison of H_2 solubility in water obtained from different models

Table 2.12. Relative difference of H_2 solubility in water obtained from different models

Temperature [°C]	Solubility [$\times 10^{-4}$ mol/m^3]	Solubility [$\times 10^{-4}$ mol/m^3]	Relative error [%]
	Gevantman [22]	Engineering toolbox [23]	
0	0.000975192	0.00096	1.56
5	0.000920734	0.00092	0.08
10	0.000875766	0.00088	0.48
15	0.000838773	0.00084	0.15
20	0.000808558	0.0008	1.06
25	0.00078417	0.00077	1.81
30	0.000764851	0.00074	3.25
35	0.000749995	0.000715	4.67
40	0.000739115	0.00069	6.65
45	0.000731823	0.00067	8.45
50	0.000727808	0.00065	10.69
55	0.000726825	0.00062	14.70
60	0.000728682	0.00059	19.03

Hydrogen diffusivity in water was measured and fitted to a correlation by Jähne et al. [24]:

$$D = 3.338 \times 10^{-6} \exp\left(-\frac{16060}{\mathrm{R}_g T}\right) \tag{13}$$

where,

D is the hydrogen diffusivity in water with the unit of m^2/s;
T is the temperature in K;
R_g is the ideal gas constant, 8.314 J/K-mol.

However, water is actually a poor solute of gaseous hydrogen. The reason behind this is that H_2 is a non-polar molecular gas, while water (H_2O) is polar molecules.

Aqueous salt solutions, such as NaCl solution, is another possible option to investigate. However, ionic salt molecules break and exit as ions once dissolving in water. The ions tend to solvate water molecules and further decrease the solubility of the nonpolar hydrogen molecules. Consequently, hydrogen solubility in aqueous solutions of salts is even lower than that in pure water. Both pure water and aqueous salt solutions are not ideal surrogates for the molten salt either.

Then the search of the solvent is switched to organic liquids. Researches have been performed for many years to develop liquid hydrogen carriers. These hydrogen carriers are originally designed for storing hydrogen as a potential green energy source. Therefore, the requirements of the hydrogen carriers include:

1. Large hydrogen storage capacity;
2. Quick absorption and desorption under reasonable conditions.

However, hydrogen carriers do not have to dissolve gaseous hydrogen physically. Hydrogen could combine with the atoms of the chemical structure and form chemical bonds or hydrogen bonds. This is the case with most organic hydrogen carriers. Since hydrogen dissolves in the molten salt physically, to simulate the real situation, it is crucial that hydrogen does not form chemical bonds with the surrogate liquid molecules.

In Table 2.13, hydrogen solubility in several organic liquids are listed and compared to that of water. The last column, desired hydrogen solubility, is the equivalent value in mole fraction to H_2 concentration in the liquid, i.e., 100 moles of hydrogen per cubic meter of solution. This value is of importance since H_2 solubility in the molten salt is of the same magnitude of 100 mol/m^3.

Table 2.13. Hydrogen solubility in organic liquids

Chemical	Molecular formula	Flammability	Molecular weight [g/mol]	Density [25°C]	Molecular density [mol/m^3]	Hydrogen solubility [mole fraction]	Desired hydrogen solubility [mole fraction] (equivalent to 100 mol H_2/m^3)
water	H_2O	N	18	1000	55555.56		0.0018
n-hexane	C_6H_{14}	Y	86.178	664.7	7713.105	0.000713	0.012965
n-octane	C_8H_{18}	Y	114.23	698.6	6115.731	0.000676	0.016351
n-decane	$C_{10}H_{22}$	Y	142.285	726.4	5105.247	0.000673	0.019588
toluene	C_7H_8	Y	92.141	873.6	9481.121	0.000315	0.010547
acetonitrile	C_2H_3N	Y	41.053	779.5	18987.65	0.000287	0.005267
acetone	C_3H_6O	Y	58.08	784.4	13505.51	0.00027	0.007404
n,n-dimethyl-formamide	C_3H_7NO	Y	73.095	944.5	12921.54	0.000184	0.007739
tetrahydrofuran	C_4H_8O	Y	72.108	882.5	12238.59	0.000141	0.008171
1,4-dioxane	$C_4H_8O_2$	Y	88.107	1028	11667.63	0.000147	0.008571
1-methyl-pyrrolodone-2	C_5H_9NO	Y	99.133	1028	10369.91	0.000178	0.009643
dibenzyltoluene	$C_{21}H_{20}$	N	272	1040	3823.529	0.003	0.026154

From Table 2.13 it can be seen that all of the candidates listed fail to have a H_2 solubility close to that of the molten salt. Most of them is an order of magnitude (in mole fraction) below what is needed, while a few are two orders of magnitudes below. Additionally, most of the candidates investigated are highly flammable, which is not ideal for laboratory experiments. Therefore, the organic surrogates are not selected for current study.

The use of carrier gas is proposed for the test of the tritium removal facility. The idea is to mix H_2 with another non-flammable gas and use the gaseous mixture instead of the molten salt. Krypton is selected as the surrogate for molten salt. The reason for selecting krypton as the carrier gas is that Kr is a major component of the reactor off gas. Additionally, it is a heavy inert gas which does not permeate through metals. Hydrogen is also a component in the off-gas from the reactor. Separation of H_2 from the other components of the off-gas has been under investigation. The experiment results of separating H_2 from Kr can also benefit the research of reactor off-gas clean-up, providing data for off-gas separation. The properties of Kr are listed in Table 2.14.

Table 2.14 Kr properties

Property	Unit	Value
Density (STP)	g/L	3.749
Molecular mass	g/mol	83.798
Heat capacity	J/kg-K	251
Thermal conductivity	W/m-K	0.00943
Viscosity	Pa-s	2.32×10^{-5}
H_2 diffusivity	m^2/s	$\frac{1.82\times10^{-6}T^{-1.564}}{\left(\ln\frac{T}{1.69\times10^{8}}\right)^{2}\exp\left(\frac{26.4}{T}\right)}$

2.7.2 Experiment setup

To take advantage of the measurement instrument (a gas chromatography) and lab space, a validation experiment of the cross-flow tritium removal facility is under construction at University of Idaho.

As explained in the previous section, the carrier gas is Kr. Nitrogen is selected to be the sweep gas in the experiment out of the consideration of achieving a good accuracy in the H_2 detection. A gas chromatograph (GC) will be used to measure the H_2 concentration in the outlet sweep gas. The GC has a thermal conductivity detector (TCD), which separate different gases according to their difference in thermal conductivities. Although helium is usually used as a sweep gas in nuclear reactor systems, its thermal conductivity is too close to that of hydrogen to be separated apart.

The scheme shown in Figure 2.19 is the proposed experiment setup. Kr and H_2 will be mixed before they enter the cross-flow facility. The gas mixture flows across the tube bank. Sweep gas, which is N_2, flows inside the tube bank. It is predicted that H_2 will permeate through the tube

walls and be carried out by the sweep gas. Samples will be collected at the outlet of the sweep gas, and analyzed. Temperatures and pressures of the inlet and outlet gases will be monitored and recorded for the accurate calculation of gas flow rates.

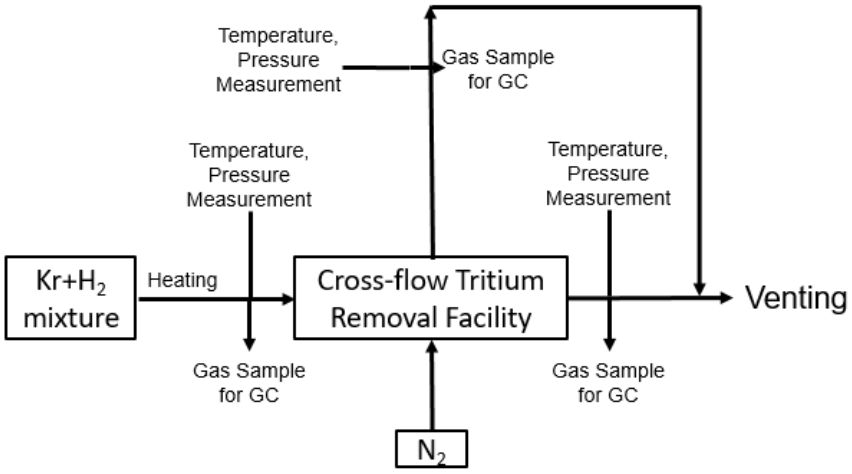

Figure 2.19 Scheme of the experiment setup

The flow diagram is shown in Figure 2.20 and a more detailed drawing is shown in Figure 2.21. The loop will be vacuumed and then charged with the mixture of H_2 and Kr. The percentage of H_2 in the gas cylinder will be in the range of 10 – 50%. The pressure of the gas mixture will be released from the high-pressure gas cylinder to slightly above the atmospheric pressure (1 - 10% above the atmospheric pressure) via a gas regulator. The gas mixture in the loop will be circulated until the concentration of H_2 in the loop cannot be detected by a gas chromatograph. During the process, H_2 will permeate into the sweep gas gradually and be vented into the hood at less than 1% hydrogen. The flow rate of the sweep gas, N_2, will vary from 30 to 500 cc/min. The pressure of the sweep gas will be slightly above the atmospheric pressure (1 - 10% above the atmospheric pressure).

Before the experiment, all the valves are closed. The Kr+H_2 line will be vacuumed. Then V2 is open while V3 is kept closed. V1 will be open and the gas mixture will fill up the loop until the pressure transducer shows the pressure in the loop is 1.0 atm. The total amount of Kr+H_2 volume is 0.5 L. Then V1 is shut off, V4 is opened, and the pump is turned on. The experiment will run for a couple of hours, while samples are taken at the outlets of the gas lines outside the glovebox. A monitor will be placed at the vent. If the H_2 concentration in the vented gas is higher than 4%, V5 will be opened and N_2 will be used to reduce the H_2 concentration. When the H_2 concentration in the out-going N_2 is lower than its detectable limit by the GC, the experiment ends. V2 is shut off and V3 is opened. Kr and the remaining H_2 (<4% concentration expected) will be vented.

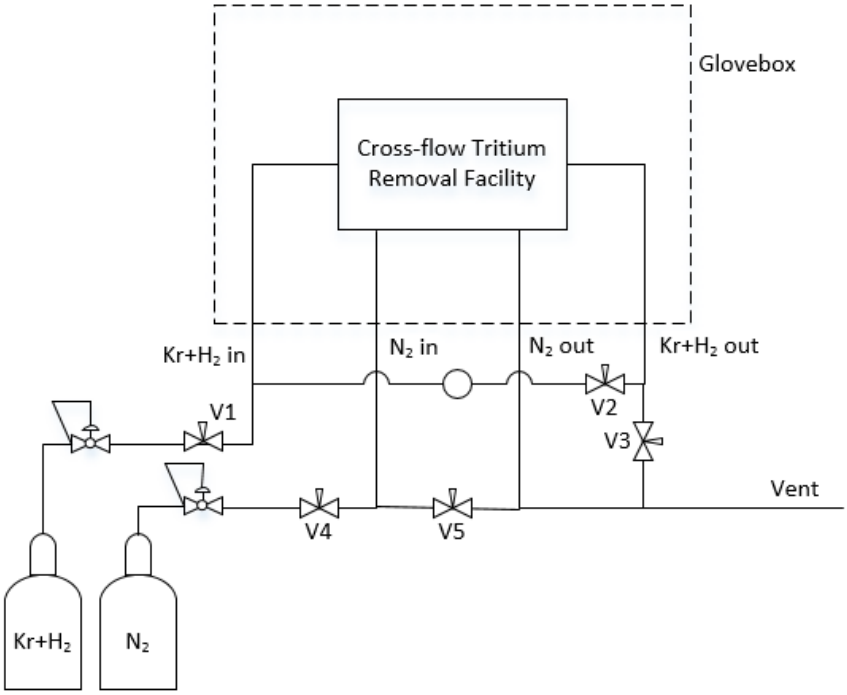

Figure 2.20 Flow diagram

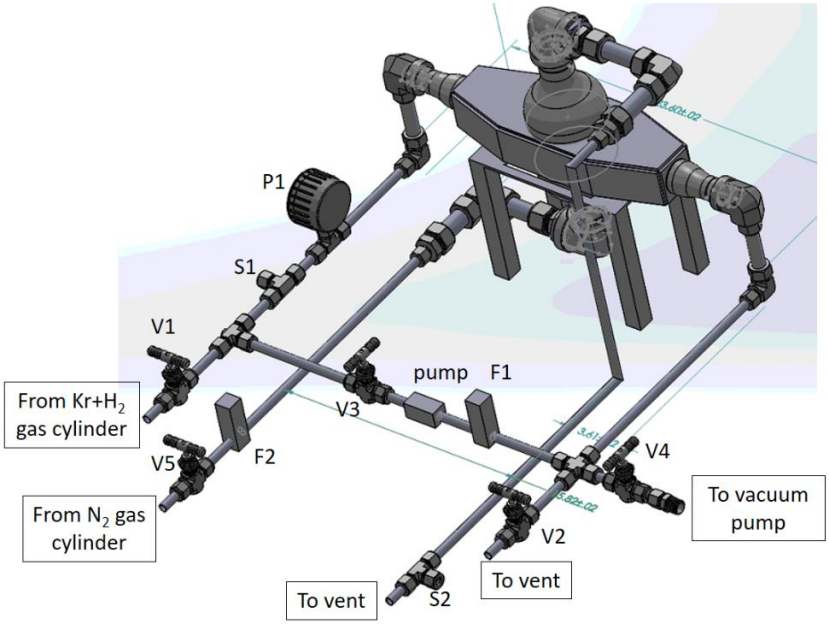

Figure 2.21 CAD drawing of the experiment setup

The section of the loop that is set up inside the glove box is mainly the small-scale cross-flow facility. Taken into consideration of the dimensions of the glove box main chamber, the connections of the facility to the tubes need to be bent, as shown in Figure 2.22. A table was built to support the weight of the facility. The completed setup is shown in Figure 2.23. For the

penetration of the four tubes in and out of the glovebox, four through holes were drilled on the back wall of the glovebox. Bored-through fittings are used with gaskets to seal the pass-throughs.

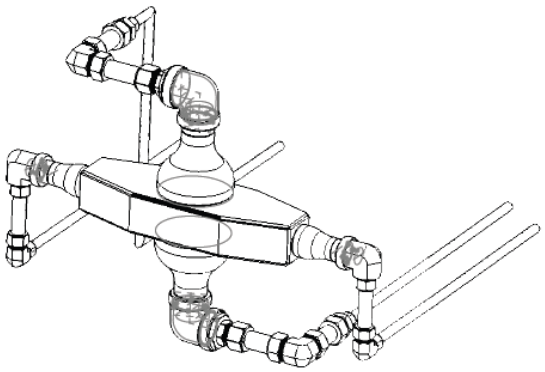

Figure 2.22 Section inside the glove box

Figure 2.23 Completed experiment setup inside glovebox

2.7.3 Fabrication of the small-scale cross-flow tritium removal facility

A small-scale cross-flow tritium removal facility was fabricated for the experiment. It is made of stainless steel 316L. The tube bank consists of 27 stagger-arranged tubes. The drawings with dimensions of the facility are shown in Figure 2.24. The tubes are half inch in size and have the wall thickness of 0.035 in. The thinnest wall thickness commercially available is used to promote hydrogen permeation. Reducers are welded on the facility as the gas inlets and outlets for smooth transitions from gas lines to the facility. For convenience connection, pipe nipples are welded on the reducers. The width of the main flow body is 6 inches, which leaves two gaps between the

side walls and the tube bank. To reduce the percentage of gas bypass from the two gaps, Trapezoidal-shaped spacers are added to the side walls. A 1-inch cylinder is also welded in front of the tube bank for the even distribution of the gas flow. It prevents the main gas stream from concentrating in the center of the tube bank.

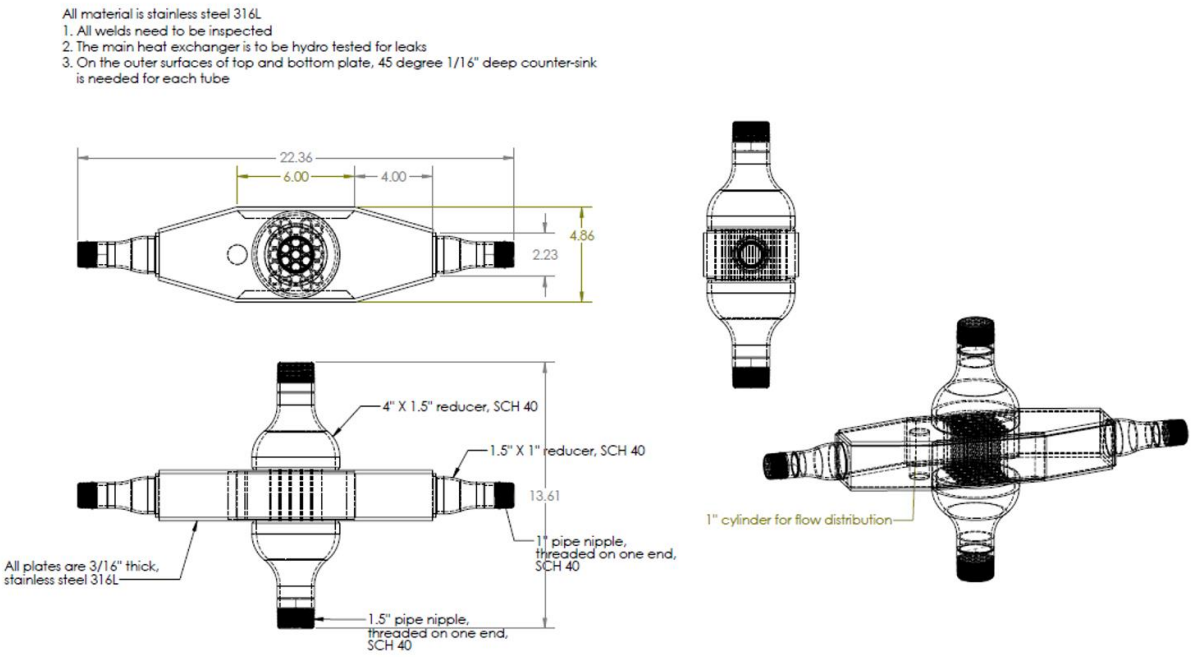

Figure 2.24 Drawings of the small-scale facility

The plates of the facility are made by laser cut, and welded together with the tube bank. Figure 2.25 shows the facility ready to be welded. Figure 2.26 shows the status of the facility after the tube bank was welded and has passed the 35-psi leakage test. The completed facility is shown in Figure 3.8. All the welds are full penetration welds.

Figure 2.25 Facility in the welding process

Figure 2.26 Facility with tube bank welded

Figure 2.27 Completed facility

2.7.4 Prediction of experiment results

The effects on the outlet H_2 concentration in sweep gas of various inlet H_2 concentrations, temperatures and gas flow rates are investigated. The calculation results are plotted in Figure 2.28-Figure 2.30. It can be observed that with the increase of inlet H_2 concentration, the outlet H_2 concentration in the sweep gas also increases. However, the increase is notable at first, and then slows down after the inlet H_2 concentration exceeds about 30%. With the increase of temperature, H_2 extraction rate slightly drops. This is because the calculation controls the flow velocity of the feed gas. Under higher temperatures, the density of the gas decreases and this leads to a decrease in the flow rate. Less amount of H_2 enters the cross-flow facility, resulting in the decrease of the outlet H_2 concentration in the sweep gas. Increase of the feed gas velocity affects the outlet H_2 concentration positively. However, similar to inlet H_2 percentage, the increase of feed gas velocity is more obvious at first. After the velocity reaches about 0.1 m/s, further increase of the feed gas velocity has limited influence on the outlet H_2 concentration in the sweep gas.

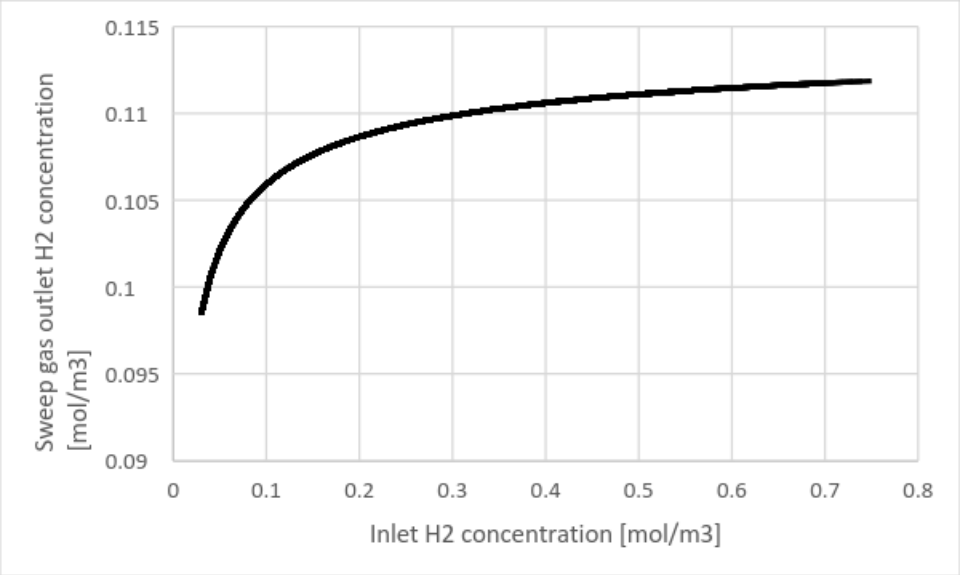

Figure 2.28 Effect of inlet H_2 percentage on outlet H_2 concentration in sweep gas

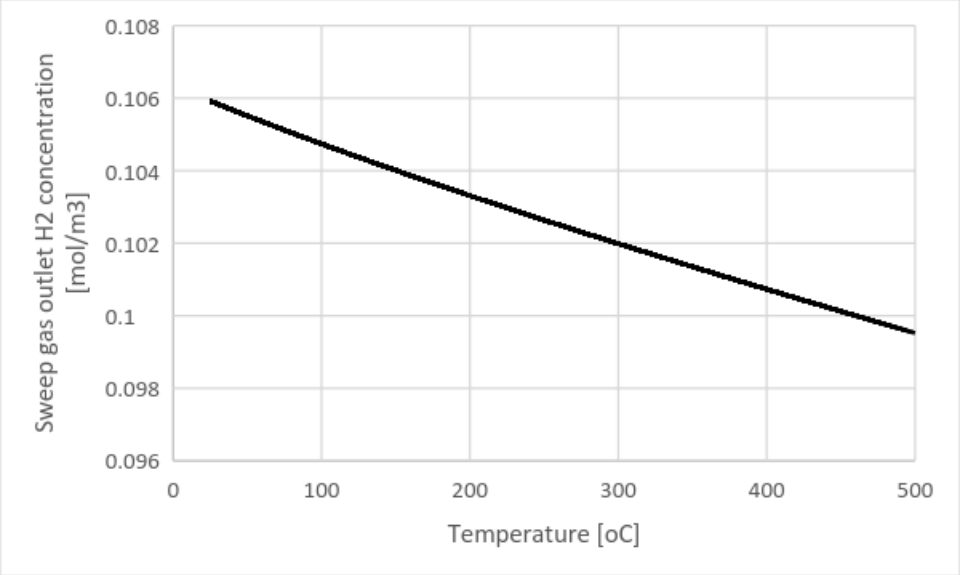

Figure 2.29 Effect of operation temperature on outlet H_2 concentration in sweep gas

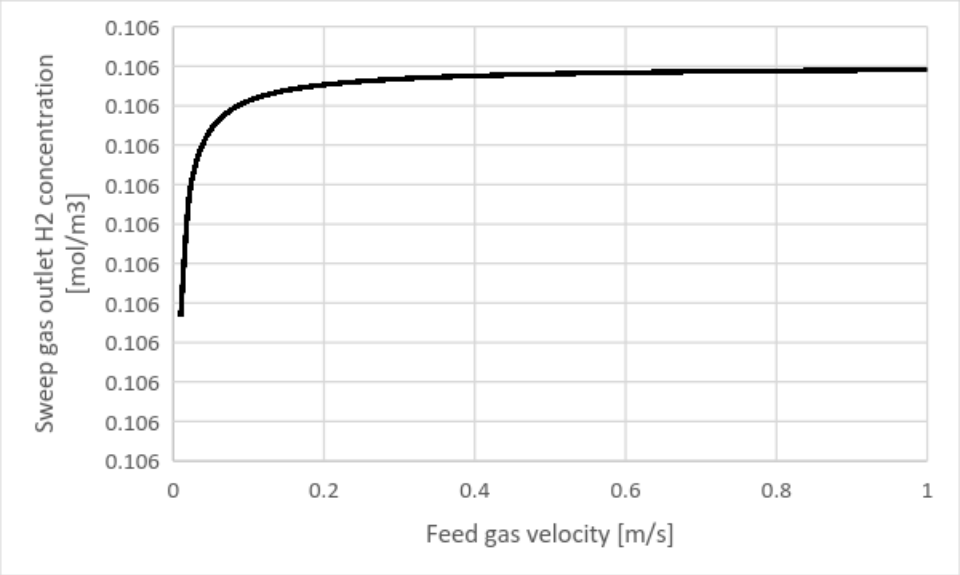

Figure 2.30 Effect of feed gas velocity on outlet H_2 concentration in sweep gas

The MATLAB calculations can be used as a guide for selection of operation conditions in the experiment. The feed gas velocity can be set at a range from 0.5 to 1 m/s. Considering the temperature features of the material, the operation temperature can vary from room temperature to moderate high temperature, for example, 300°C. The inlet H_2 percentage can vary from <3% to 30%.

2.8 Validation experiment using molten salt

For the experiment using molten salt as the H_2 carrier, the schematic of the loop is shown in Figure 2.31. FLiNaK is pumped through a loop, which consists of a H_2 dissolution station and a small-scale removal facility. The H_2 carried out by the purging gas from the removal facility is quantitatively analyzed by a hydrogen sensor. At equilibrium, the rate of H_2 dissolving into FLiNaK equals the H_2 flow rate at the molten salt inlet of the removal facility. By recording the H_2 flow rate in the outlet purging gas during the steady state operation, the overall mass transfer coefficient of the experiment facility can be calculated. The results can be scaled up to obtain the removal effectiveness for the full-scale tritium removal facility.

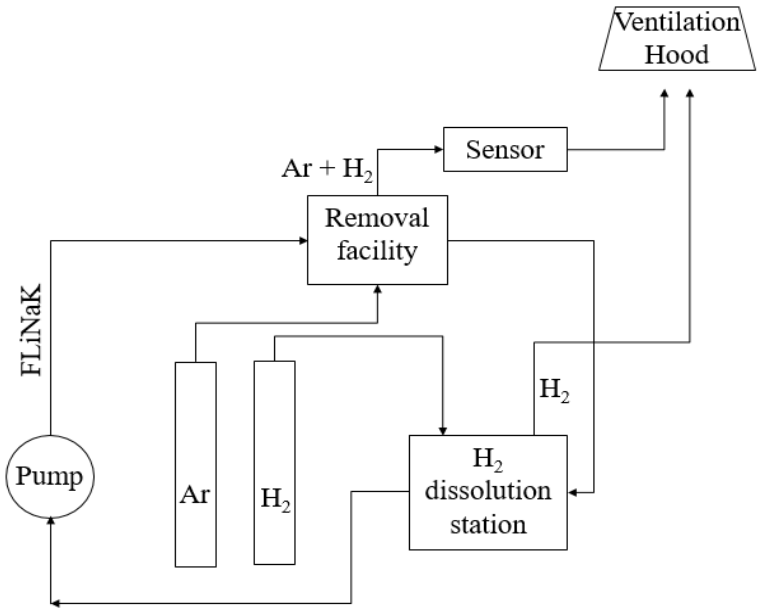

Figure 2.31 Schematic of the H_2 removal validation experiment with molten salt

As shown in Figure 2.31, the experiment consists of a molten FLiNaK loop, a H_2 loop, and an Ar purging gas loop. Molten salt is driven through the loop by a pump. It picks up H_2 at the H_2 dissolution station, and flows across the tube bank in the removal facility. Part of the H_2 dissolved in the FLiNaK is removed in the removal facility. Ar is used as the purging gas in this experiment. It flows through the tube bank of the removal facility and carries away the H_2 transporting out of the FLiNaK. The outlet Ar with H_2 will go through a H_2 sensor, which is a gas chromatography, and the concentration of H_2 will be measured and recorded. The mixed gas is then vented out through a ventilation hood.

Figure 2.32 shows the CAD drawing of the test section of molten salt. This experiment will take advantage of the FLiNaK loop in the lab, which is designed to investigate the performance of DRACS in FHRs [25]. The test section shown here will be connected to the existing loop via flanges. The experiment loop section will share pumps, heaters, flowmeters, thermocouples and pressure transducers with the existing High Temperature DRACS Test Facility (HTDF). NPS 1.5'' stainless steel 316H pipes will be used to match existing facility pipes. Thermal insulation will be applied around the pipes and facilities to avoid salt freezing due to heat loss. The main facilities in the testing loop are the H_2 addition facility and the H_2 removal facility. The two are identical in geometry and are connected together by flanges. The short distance between the two facilities is intended to minimize the H_2 leakage from the molten salt. An ultrasonic flowmeter will be installed on the loop to monitor the molten salt flow rate. To avoid molten salt leakage, flanges and elbows will be directly welded to the pipes.

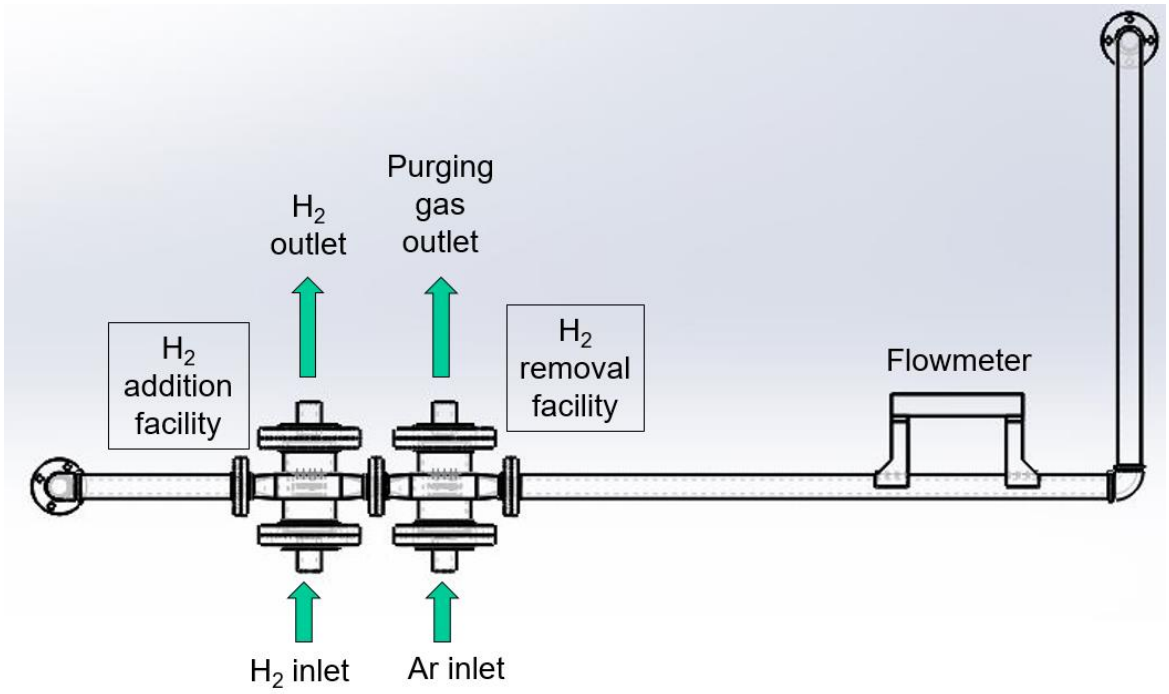

Figure 2.32 Design of test section in the molten salt loop

The gas lines are shown in Figure 2.33 and Figure 2.34. The H_2 addition gas line goes through the H_2 addition facility. The Ar purging gas line goes through the H_2 removal facility. Per the current lab arrangement, there will be a considerable distance between the gas cylinders and the testing loop. In addition, it's always safer for gas cylinders to be located at certain distance away from the high temperature molten salt test facilities. Hoses and ¼-inch tubes will be used to connect gas cylinders and the facilities. Table 2.15 explains the components of the loops.

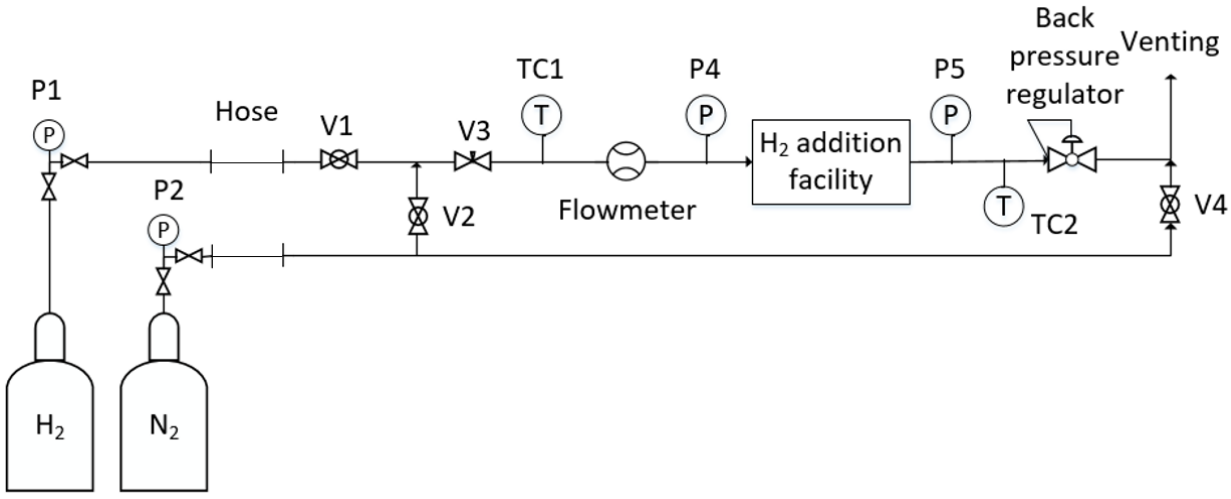

Figure 2.33 Schematic of the H_2 addition gas line

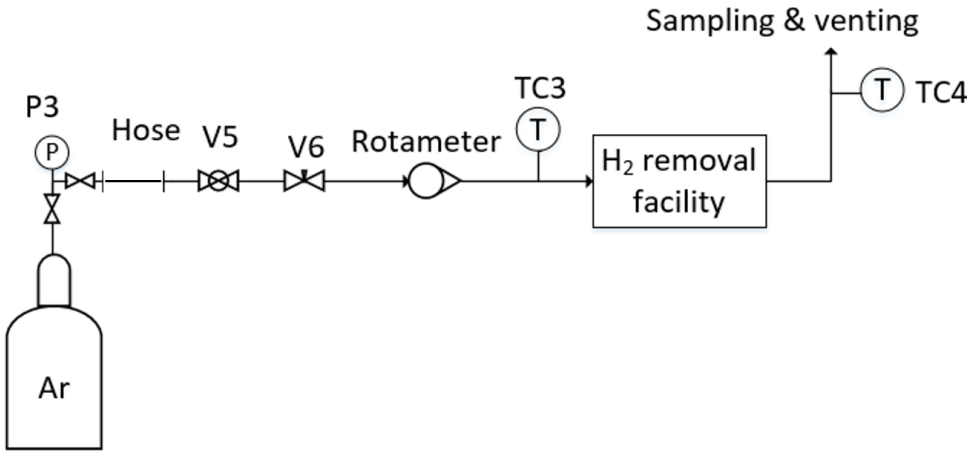

Figure 2.34 Schematic of the Ar purging gas line

Due to the delay of loop construction, the experiment using molten salt has not been setup. However, in the future, if permitted, the experiment will be setup and carried out. Computer simulation of the experiment will be performed, and the experimental data and the simulation results will be compared.

Table 2.15 Table of loop components

Denotation	Component type	Location	Function
V1	Ball valve	H_2 addition gas line	Shut-off valve for H_2 gas cylinder
V2	Ball valve	H_2 addition gas line	Shut-off valve for N_2 gas purging line
V3	Needle valve	H_2 addition gas line	Control and adjust H_2/N_2 flow rate
V4	Ball valve	H_2 addition gas line	Shut-off valve for N_2 gas venting line
V5	Ball valve	Ar purging gas line	Shut-off valve for Ar gas cylinder
V6	Needle valve	Ar purging gas line	Control and adjust Ar flow rate
TC1	Thermocouple	H_2 addition gas line	Monitor and record H_2/N_2 temperature near the Flowmeter
TC2	Thermocouple	H_2 addition gas line	Monitor and record H_2/N_2 temperature near P5
TC3	Thermocouple	Ar purging gas line	Monitor and record Ar temperature near the Rotameter
TC4	Thermocouple	Ar purging gas line	Monitor and record out-coming purging gas temperature near the sampling station
P1	Pressure regulator	H_2 addition gas line	Pressure regulator for H_2 gas cylinder
P2	Pressure regulator	H_2 addition gas line	Pressure regulator for N_2 gas cylinder
P3	Pressure regulator	Ar purging gas line	Pressure regulator for Ar gas cylinder
P4	Pressure transducer	H_2 addition gas line	Monitor and record H_2 gas line pressure before the H_2 addition facility
P5	Pressure transducer	H_2 addition gas line	Monitor and record H_2 gas line pressure after the H_2 addition facility
Back pressure regulator	Pressure regulator	H_2 addition gas line	Control H_2/N_2 loop pressure (coupling with P1/P2); release pressure before exhausted gas being vented
Flowmeter	Flowmeter	H_2 addition gas line	Monitor and record H_2/N_2 flow rate
Rotameter	Flowmeter	Ar purging gas line	Monitor and record Ar flow rate
Hose	Flexible hose	Ar purging gas line	Connect gas cylinders and main loops

3. Development of a Tritium Analysis Code

To further evaluate the tritium removal efficiency of the designed cross-flow tritium removal facility, development of a tritium analysis code is necessary. Due to the similarity of mass transport and heat transfer, the heat transfer calculation methods are reviewed. In heat transfer calculation, two types of methods have been used. One is to divide the volume into meshes and solve for each mesh, and the other is to use a 0-D, "black box" method based on a mean temperature difference. The former can be applied to mass transfer calculation directly, but the latter needs some modification, especially when calculation interphase gas diffusion.
The two-film theory for interphase mass transfer shows that concentration can "jump" at the interface of two materials, but the partial pressure is continuous [21]. Therefore, the variable that corresponds to temperature should be partial pressure of the diffusing material. Then the log mean temperature difference (LMTD) should be modified to log mean partial pressure difference (LMSPD).

Besides, one of the difficulties in the 0-D overall mass transfer calculation method is the case of gas diffusing through metal. This difficulty mainly comes from the solubility. Henry's law shows that solubility is proportional to the partial pressure of the solute gas, if the solvent is salt, for example, FLiBe. Sievert's law predicts that the solubility is proportional to the square root of the partial pressure of the solute gas, of the solvent is metal. Therefore, special attention must be paid when deriving the overall mass transfer coefficient.

3.1 Derivation of tritium mass transfer calculation method

In Figure 3.1, a unit of interphase gas transferring is shown. Take the case of a bimolecular gas diffusing from fluid 1 to fluid 2 as an example. Correspondence between the concentration of the gas and the corresponding partial pressure is shown in Table 3.1.

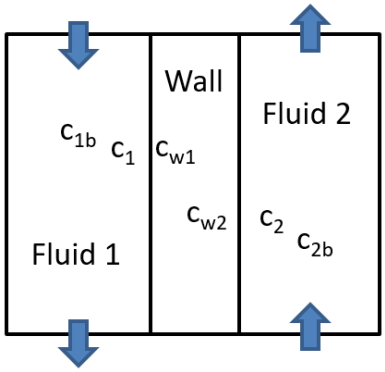

Figure 3.1. Mass transfer unit

Table 3.1. Variables in the mass transfer unit

	Concentration	Partial pressure
Fluid 1 bulk	c_{1b}	p_{1b}
Fluid 1 wall surface	c_1	p_1
Wall inside surface fluid 1 side	c_{1w}	p_{1w}
Wall inside surface fluid 2 side	c_{2w}	p_{2w}
Fluid 2 wall surface	c_2	p_2
Fluid 2 bulk	c_{2b}	p_{2b}

The diffusion of H_2 from primary coolant main stream to the inner surface of the wall can be written as Equation (14):

$$Q = h_1 A_1 \left(c_{1b} - c_{1w} \right) \tag{14}$$

where,

Q is the mass transfer rate;

A_1 is the mass transfer area;

c_{1b} and c_{1w} are the T_2 concentrations in the main stream and at the tube wall surface, respectively.

$$Q = h_1 A_1 H_1 \left(p_{1b} - p_{1w} \right) \tag{15}$$

$$Q = h_1 A_1 H_1 \left(\sqrt{p_{1b}} + \sqrt{p_{1w}} \right)\left(\sqrt{p_{1b}} - \sqrt{p_{1w}} \right) = h_{1p} A_1 \left(\sqrt{p_{1b}} - \sqrt{p_{1w}} \right) \tag{16}$$

$$Q = D_w \frac{2\pi L}{\ln\left(\frac{d_{1o}}{d_{1i}} \right)} \left(c_{1w} - c_{2w} \right) = D_w \frac{2\pi L}{\ln\left(\frac{d_{1o}}{d_{1i}} \right)} S_w \left(\sqrt{p_{1w}} - \sqrt{p_{2w}} \right) \tag{17}$$

$$\begin{aligned} Q = h_2 A_2 \left(c_{2w} - c_{2b} \right) = h_2 A_2 H_2 \left(p_{2w} - p_{2b} \right) &= h_2 A_2 H_2 \left(\sqrt{p_{2w}} + \sqrt{p_{2b}} \right)\left(\sqrt{p_{2w}} - \sqrt{p_{2b}} \right) \\ &= h_{2p} A_2 \left(\sqrt{p_{2w}} - \sqrt{p_{2b}} \right) \end{aligned} \tag{18}$$

The overall mass transfer equation has the form of

$$Q = h_o A_1 \left(\sqrt{p_{1b}} - \sqrt{p_{2b}} \right) \tag{19}$$

Combining Equations (15)-(19), the overall mass transfer coefficient is

$$h_o = \frac{1}{\frac{1}{h_{1p} d_{1i}} + \frac{\ln\left(\frac{d_{1o}}{d_{1i}}\right)}{2P_w} + \frac{1}{h_{2p} d_{1o}}} \frac{1}{d_{1i}} \tag{20}$$

The difference of square roots of partial pressures in Equation (21) can be estimated by the log mean difference of partial pressures in the main streams of the two fluids:

$$\sqrt{p_{1b}} - \sqrt{p_{2b}} = LMPD = \frac{\left(\sqrt{p_{1i}} - \sqrt{p_{2o}}\right) - \left(\sqrt{p_{1o}} - \sqrt{p_{2i}}\right)}{\ln\left(\frac{\sqrt{p_{1i}} - \sqrt{p_{2o}}}{\sqrt{p_{1o}} - \sqrt{p_{2i}}}\right)} \tag{21}$$

Mass transfer coefficients in the fluids can be calculated using Sherwood number.

$$\mathrm{Sh} = \frac{h_i d_{hi}}{D_i}, \; i = 1 \text{ or } 2 \tag{22}$$

The Sherwood number itself can be calculated using correlations developed for heat transfer calculations, but with the Nu replaced with Sh and Pr replaced with Sc, as shown in Equation (23).

$$\mathrm{Sh} = \begin{cases} 0.4\,\mathrm{Re}^{0.6}\,\mathrm{Sc}^{0.36} & \text{for } \mathrm{Re} = 1000 - 20000 \\ 0.022\,\mathrm{Re}^{0..84}\,\mathrm{Sc}^{0.36} & \text{for } \mathrm{Re} > 20000 \\ 3.41 & \text{for } \mathrm{Re} < 1000 \end{cases} \tag{23}$$

An iteration loop can be written to calculate the mass transfer rate. The logic of the loop is:

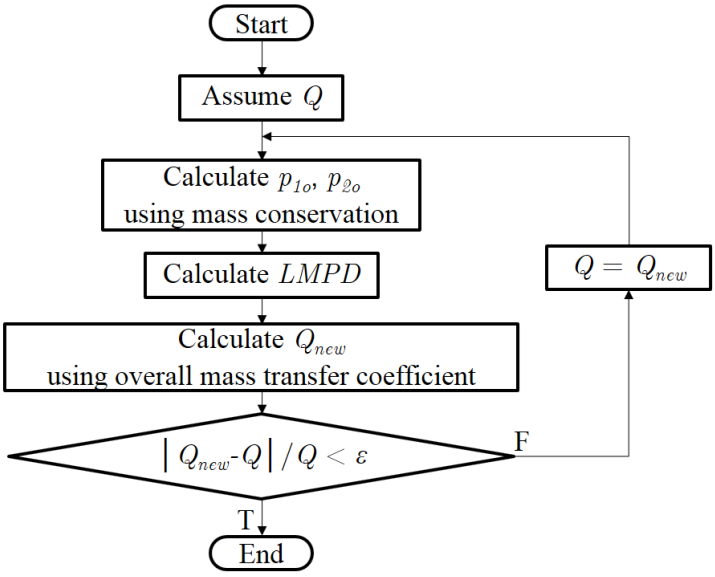

3.2 Comparison with experimental data

For the verification of the developed code, a model of H_2 permeating through a Ni tube has been built and calculated. The model is based on the H_2 permeation experiment performed by Wang et al. [26]. A hollow fiber made of Ni was heated to different temperatures from 400 °C to 1000 °C. The feed gas, which is a mixture of H_2 with the carrier gas, flows on the shell side, while the purging gas N_2 flows on the tube side of the Ni fiber in the co-current direction with H_2. H_2 concentration on the shell side is controlled by adjusting the ratio of H_2 in the feed gas. As Ni has high hydrogen selectivity, H_2 will diffuse from the shell side, permeate through the wall, and enter the tube side. Outlet gases were analyzed using a gas chromatography to determine the partial pressure difference between the two sides.

The schematic diagram of the experiment is shown in Figure 3.2. The inner diameter and outer diameter of the permeation tube are 1.33 mm and 2.00 mm, respectively. Effective length of the permeation section is 8 cm. Flow rates of gases on both sides are 30 ml/min. Mass flow rates and velocities of both gases will vary with different experimental temperatures. For the modeling, permeability of H_2 through Ni used is the value provided in the paper, which is $P_{Ni,H} = 1.44\times10^{-6}\exp\left(-\frac{5.107\times10^{4}}{RT}\right)$ [26]. Hydrogen diffusion in gases are also considered in the model. The carrier gas selected in the model is CO_2, and the molar percentage of H_2 on the shell side inlet is 50%.

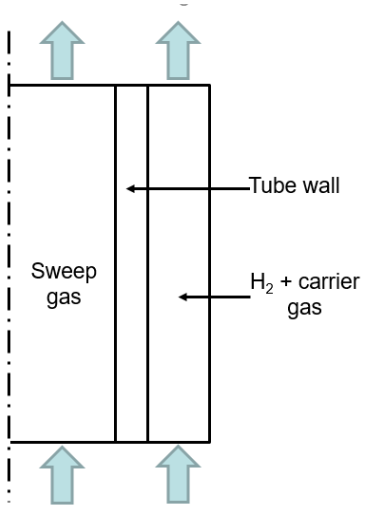

Figure 3.2 Diagram of counter-current flow model

Transport coefficients, i.e., diffusivity and solubility, of H_2 in CO_2 and N_2 are summarized in Table 3.2. Assuming all gases are ideal gas, and therefore, solubility of H_2 in another gas can be estimated using the ideal gas law.

Table 3.2 Transport coefficients of H_2 in CO_2 and N_2

	Diffusivity [atm-m^2/s] [27]	Solubility [mol/m^3-Pa]
CO_2	$D_{CO_2,H} = \frac{3.14\times10^{-9}T^{1.750}}{\exp\left(\frac{11.7}{T}\right)}$	$S_{CO_2,H} = \frac{n}{pV} = \frac{1}{RT}$
N_2	$D_{N_2,H} = \frac{1.539\times10^{-6}T^{1.548}}{\left[\ln\left(\frac{T}{3.16\times10^{-7}}\right)\right]^2 \exp\left(-\frac{2.8}{T}\right)\exp\left(\frac{1067}{T^2}\right)}$	$S_{N_2,H} = \frac{n}{pV} = \frac{1}{RT}$

The calculated H_2 permeation flux under different temperatures is plotted against the difference of square root of partial pressure $\Delta p^{0.5}$ in Figure 3.3.

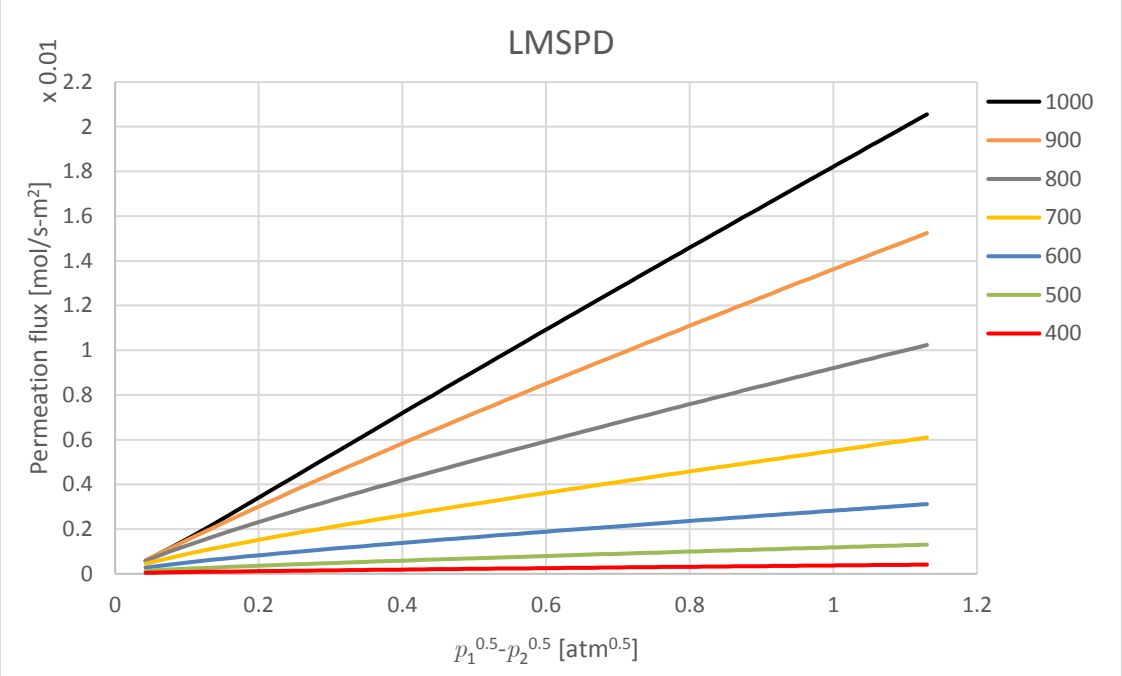

Figure 3.3 Code calculation results from LMSPD method

The same model was also calculated by a conventional mass transfer code, where the geometry was divided into segments and local mass balance was forced. This code is referred to as the "meshed method" in this paper. In the meshed method, permeation is one dimensional from the tube wall outer surface (shell side) to the inner surface (tube side). It is assumed that the concentration profile in both carrier gas and seep gas is flat. That is, the gradient of H_2 partial pressure exits only in the tube wall. The tube wall is divided into segment only in the axial direction, and not in the radial direction. The results are plotted in Figure 3.4.

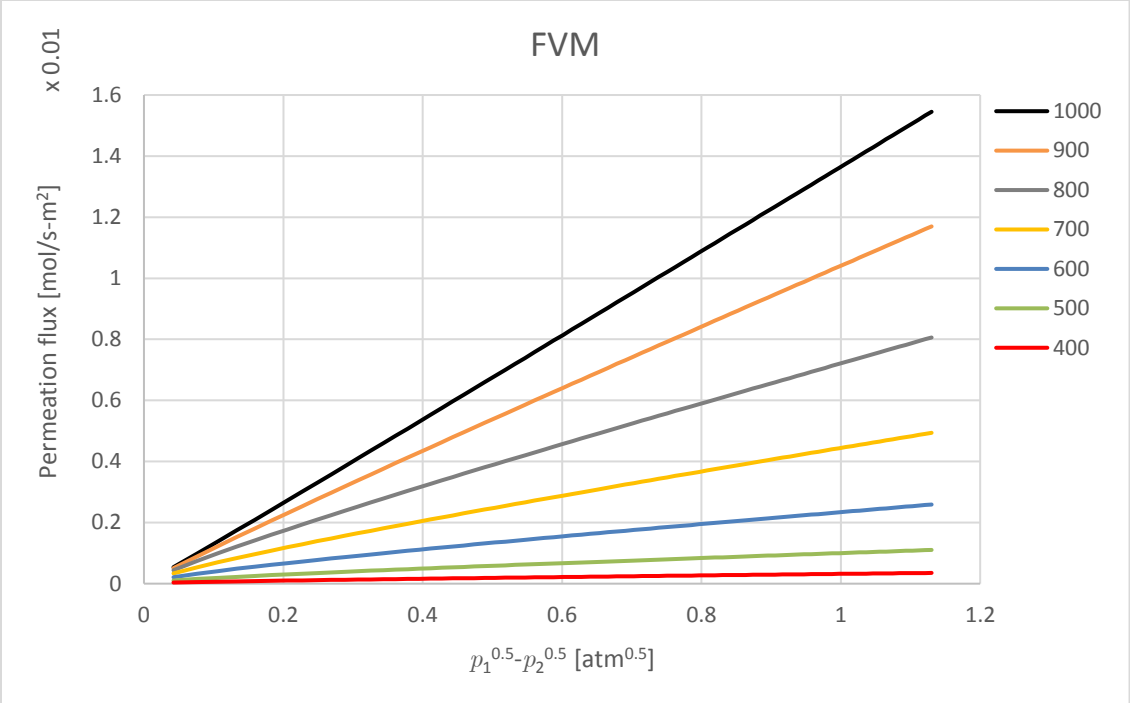

Figure 3.4 Code calculation results from meshed method

The experimental data were shown in Figure 3.5. In this plot, the partial pressures used in the x-axis are calculated from concentration measurements at the gas outlets. The points are original data, while the lines are fitted linear trend lines [26].

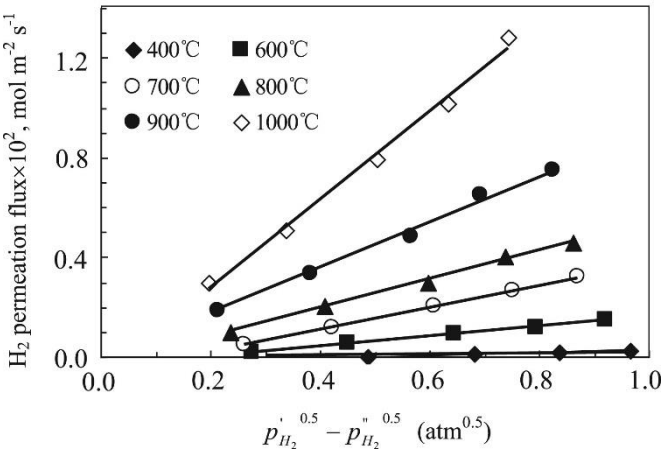

Figure 3.5 Experimental data [26]

COMSOL simulation of the experiment was also performed. An axisymmetric model was built using COMSOL Multiphysics. The geometry and domains as set as shown in Figure 3.2. Physics modules used in the model are turbulent flow and transport of diluted species. The model was solved using stationary solvers. The two turbulent flow modules were solved first using a segregated and direct solver, and the three mass transport modules were solved using a fully

coupled and direct solver. The velocity field obtained from the first step was used as the initial conditions in the second step.

On the interfaces between fluids and the wall, pointwise constraints were used to force the flux to continue while allow the concentration to jump [28].

Permeation flux at 1000°C obtained from the two codes are compared with the experimental data in Figure 3.6. In general, the LMSPD method overestimates the permeation flux, while the meshed method underestimates it. The difference between LMSPD method results and experimental data varies from 5.9% to 19.0%. The difference between meshed method results and experimental data varies from 10.6% to 21.1%.

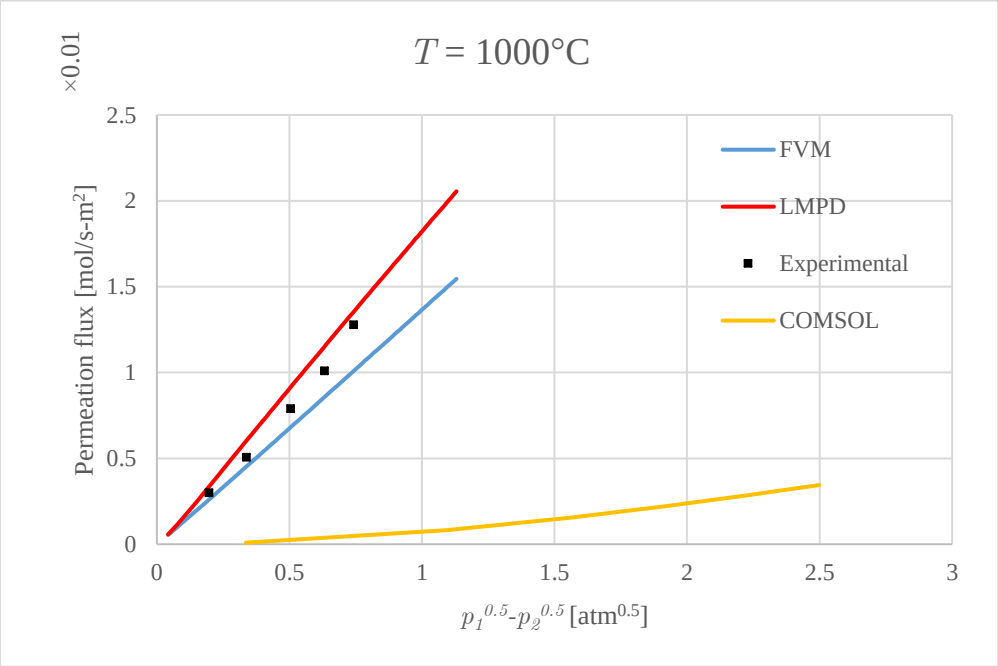

Figure 3.6 Comparison of calculation results at 1000 °C

For lower temperatures, both codes tend to overestimate the permeation flux, as shown in Figure 3.7 where the calculation results and experimental data were compared at 600 °C. Also, the difference between the calculation results and the experimental data were apparently larger than at higher temperatures. For lower differences of square root of partial pressure, the code calculation results could be as high as twice or three times of the experimental results.

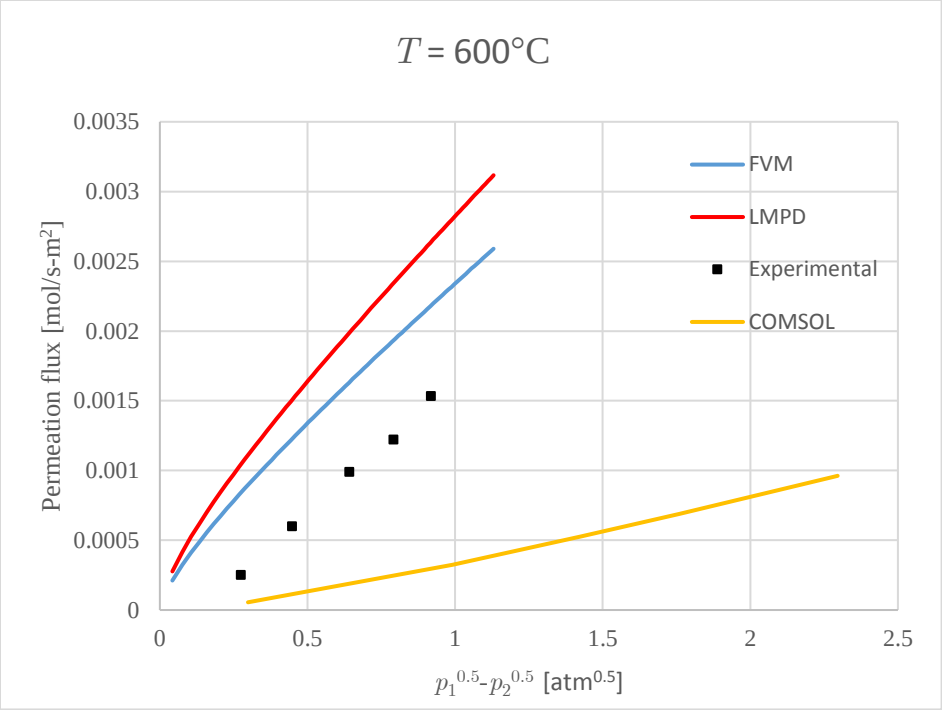

Figure 3.7 Comparison of calculation results at 600 °C

3.3 Discussion of simulation results

3.3.1 Difference between code calculation and experimental data

The absolute and relative differences between the code calculation and experimental data are shown in Table 3.3. The difference is larger at lower temperatures and smaller driving forces, i.e., the difference of square roots of partial pressures on both sides. Several reasons might have caused this increased difference. Comparing the absolute difference between code calculation results and the experimental data, it can be found that the value always falls in the 10^{-4}-10^{-3} magnitude range. The relative difference, however, becomes significant when the permeation flux is low. Additionally, at lower temperatures, the permeability of hydrogen through nickel wall decreases, and therefore, the amount of hydrogen permeating through the wall is less than that at higher temperatures. Smaller driving forces also lead to lower hydrogen permeation. The error of measurement could be more obvious when the concentration is low.

Table 3.3 Difference between code results and experimental data

Temperature	Code	Type	Min. difference	Corresponding $p_1^{0.5}$-$p_2^{0.5}$ [atm$^{0.5}$]	Max. difference	Corresponding $p_1^{0.5}$-$p_2^{0.5}$ [atm$^{0.5}$]
1000°C	LMSPD	Absolute	3.58×10^{-4}	0.20	1.43×10^{-3}	0.63
		Relative	5.91%	0.74	19.0%	0.34
	FVM	Absolute	3.92×10^{-4}	0.20	2.69×10^{-3}	0.74
		Relative	10.6%	0.34	21.1%	0.74
600°C	LMSPD	Absolute	7.94×10^{-4}	0.27	1.12×10^{-3}	0.79
		Relative	72.0%	0.92	318%	0.27
	FVM	Absolute	5.90×10^{-4}	0.27	7.13×10^{-4}	0.79
		Relative	42.3%	0.92	236%	0.27

3.3.2 Difference between COMSOL simulation and experimental data

COMSOL simulation results are one magnitude or more lower than either code calculation results or experimental data. The difference might come from the different approaches at dealing with interface boundary conditions. In COMSOL, the pointwise constraint condition does not model the flux, but assign a concentration value to the downstream side. A parameter named partition factor is used to define the jump of concentration across the boundary. The definition of partition factor is the ratio of concentrations in two different and immiscible phases at equilibrium [29], as shown in Equation (24).

$$P_{AB} = \frac{c_B}{c_A} \tag{24}$$

For the interface of feed gas and wall, the partition factor should be:

$$P_{1w} = \frac{c_{w1}}{c_{1w}} = \frac{K_w\sqrt{p_{1w}}}{K_1 p_{1w}} = \frac{K_w}{K_1\sqrt{p_{1w}}} = \frac{K_w}{\sqrt{K_1 c_{1w}}} \tag{25}$$

Similarly, the partition factor for the interface of wall and sweep gas can be written. Therefore, the partition factor is dependent on the concentration of hydrogen in the fluids, and could vary with location. However, in most cases, the partition factor is known beforehand, often obtained via experiments or atom-based calculation [30]. Estimating the partition factor during the simulation process might be inaccurate.

Additionally, in COMSOL, diffusivities in each material must be input. The experiment modeled only provided hydrogen permeability through the nickel wall. While the exact diffusivity of the nickel wall used in the experiment is unknown, a value from literature was used in the simulation. This estimation will also lead to inaccuracy in the permeation flux.

Mesh size may also play a significant role in the accuracy of results. In this study, the mesh size used was “normal” and the sequence type was “physics-controlled mesh” by COMSOL

presetting. For mass transfer, finer mesh is ideal. But because of the limited computational resources finer mesh was not adopted here.

3.3.3 Permeation flux and the difference of square root of partial pressure

The mass transfer coefficients of H_2 in all three domains are compared in Table 3.4. The mass transfer coefficient in the tube wall is several magnitudes lower than that in the sweep gas or the carrier gas, showing that the main resistance exits in permeating through the tube wall. In the meshed method, only the permeation through wall is considered. However, because of the significant difference of mass transfer coefficients in different domains, omitting the mass transfer resistance in gases does not have a significant effect on the calculation results.

Table 3.4 Comparison of mass transport coefficients in different domains

Temperature [°C]	$p_1^{0.5}$-$p_2^{0.5}$ [atm$^{0.5}$]	Mass transfer coefficient [mol/m^2-s-Pa]		
		Feed gas	Wall	Sweep gas
1000	0.125	0.0058	8.53×10^{-8}	2.27×10^{-4}
	2.023	0.0155	2.08×10^{-8}	9.32×10^{-4}
600	0.656	0.0080	1.04×10^{-9}	3.56×10^{-4}
	2.595	0.0196	2.78×10^{-10}	0.0013

The permeation flux is directly related to the difference of square roots of partial pressures on both sides. The linearity of the slopes in Figure 3.3 and Figure 3.4 are quite good, and should be in the form of Equation (26). Fitting the code results in Figure 3.6 and Figure 3.7 to linear relationships with $\left(\sqrt{p_1}-\sqrt{p_2}\right)$, the obtained correlation and R^2 values are listed in Table 3.5. This is in consistence with what is predicted in the Sievert's equation [31], showing that the assumption of diffusion in the wall being the rate-dominating step is reasonable.

$$J=\frac{P_{Ni,H}}{\delta}\left(\sqrt{p_1}-\sqrt{p_2}\right) \tag{26}$$

Table 3.5 Correlations of permeation flux and difference of square roots of partial pressures

Temperature [°C]		600
LMSPD	Correlation	$J = 0.0025\left(\sqrt{p_1} - \sqrt{p_2}\right) + 0.0004$
	R^2	0.9972
Meshed	Correlation	$J = 0.0021\left(\sqrt{p_1} - \sqrt{p_2}\right) + 0.0003$
	R^2	0.9977
Temperature [°C]		1000
LMSPD	Correlation	$J = 0.0184\left(\sqrt{p_1} - \sqrt{p_2}\right) - 0.0002$
	R^2	0.9999
Meshed	Correlation	$J = 0.0138\left(\sqrt{p_1} - \sqrt{p_2}\right) - 0.0001$
	R^2	1

4. IHX Design as a Companion Facility for the Tritium Removal Facility

In the primary loop of a FHR, the intermediate heat exchanger (IHX) is located after the tritium removal facility. Due to the high level of tritium concentration in the primary coolant, a tritium diffusion barrier might be needed to prevent tritium from leaking into the secondary loop through the IHX tubes. The barrier must be located between the primary loop and the secondary loop, which means that the barrier would also participate in the heat transfer. Therefore, in designing and optimizing the IHX with tritium permeation barrier, heat transfer resistance added to the IHX due to the added barrier need to be balanced with the tritium permeation reduction performance.

The geometry of such a heat exchanger with barrier would be a normal tube-and-shell heat exchanger. A single tube unit is shown in Figure 4.1. Primary coolant flows inside Tube 1. Right outside each tube, there is a concentric tube (Tube 2) which sandwiches the tritium permeation barrier between itself and the primary side tube (Tube 1). The secondary coolant flows in the gap between Tube 2 and Tube 3. In Table 4.1 the design parameters are listed.

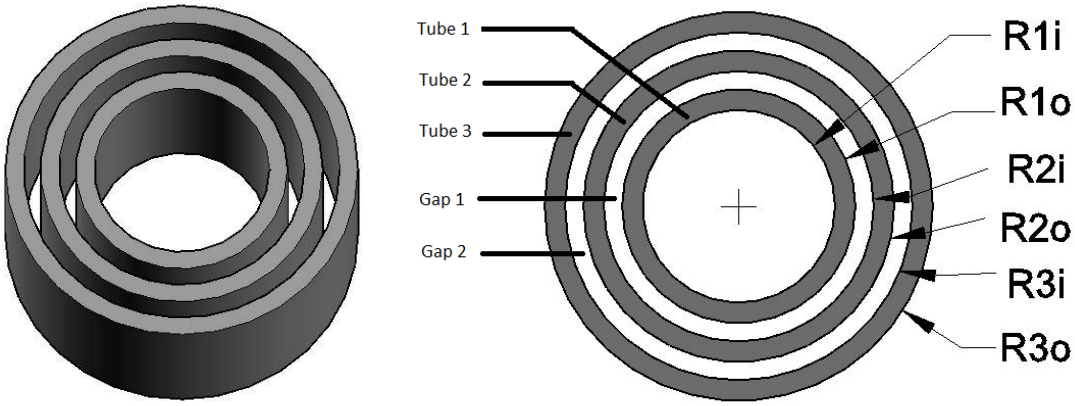

Figure 4.1 Intermediate heat exchanger with tritium permeation barrier

Table 4.1 Primary parameters of the IHX with barrier

Inner radius of Tube 1 (R1i) [mm]	12.7	Outer radius of Tube 1 (R1o) [mm]	13.4
Tube wall thickness [mm]	0.737	Gap 2 thickness [mm]	6.35
Barrier thickness [mm]	~ 1	FLiNaK barrier flow rate [m/s]	0.05
Primary coolant flow rate [m/s]	0.5	Secondary coolant flow rate [m/s]	0.5

As shown above in Table 4.1, molten salts are good tritium diffusion barriers. Thus one proposed design is to use FLiNaK, which has a lower tritium diffusion coefficient than FLiBe, as the tritium permeation barrier. FLiNaK is designed to flow at a very low speed, for instance, 1/10 of

the FLiBe flow rate. An intermediate heat exchanger using molten salt as the tritium permeation barrier will have a similar structure as is shown in Figure 4.2.

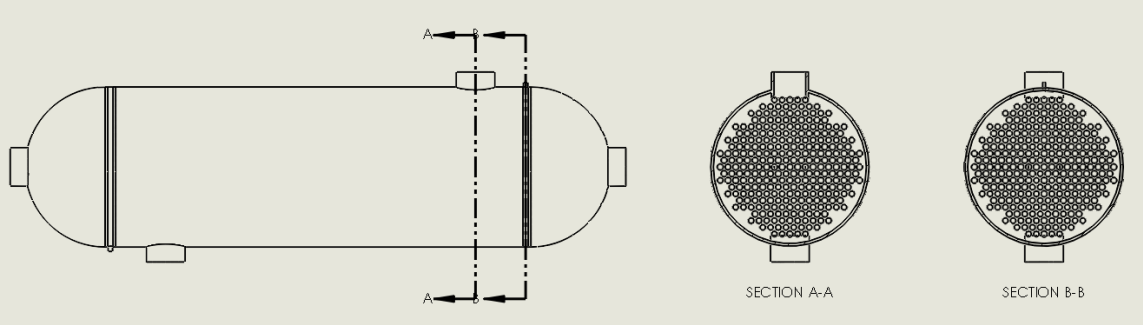

Figure 4.2 Structure of an IHX using molten salt as tritium permeation barrier

Another design proposed is to use Al_2O_3, which is widely studied as promising tritium permeation barrier material, as the sandwiched tritium permeation barrier in the intermediate heat exchanger. The only difference of this design compared to the one above is that FLiNaK is replaced by Al_2O_3. According to literature, a major application of Al_2O_3 is to apply it as a coating on surfaces. However, one of the main issues with Al_2O_3 coating is that it is difficult to produce uniform coating without defects. Defects in the coating would greatly reduce its effectiveness as tritium permeation barrier. Also the coating cracks under irradiation and corrosion, which again derogates its permeation reduction performance significantly. However, in this proposed geometry, Al_2O_3 is sandwiched between two tubes. In this way, Al_2O_3 distributes uniformly around the inner tube. As long as thermal expansion or deformation due to radiation does not exceed the crack limits of Al_2O_3, this "coating" has little defects that would damage the performance of tritium permeation barrier.

Compared to FLiNaK, Al_2O_3 has a higher thermal conductivity. Thermal conductivity of FLiNaK is around 1 W/m-K, while that of Al_2O_3 is around 30 W/m-K. Therefore, the heat transfer performance is better with the Al_2O_3 barrier, if both barriers are of the same thickness. Current concern of the Al_2O_3 design is that the barrier may reach saturation in a certain time length after the operation starts. Unlike FLiNaK or other type of molten salt tritium permeation barrier which can flow and get cleaned up, Al_2O_3 barrier are expected to last long before getting replaced. It still remains to be examined whether Al_2O_3 can still act as satisfactory tritium permeation barrier in an intermediate heat exchanger, even when it is saturated with tritium. Additionally, the integrity of the barrier is a key factor in the tritium permeation reduction performance of the Al_2O_3 barrier. Under the high temperature gradient in the IHX, it is highly possible that the barrier will develop cracks which degrades the tritium permeation reduction performance.

5. Economic Assessment

One of the objectives of this study is to show the economic advantages the two-loop FHR design holds compared to the three-loop design. To evaluate the cost of both systems, economic analysis of the cross-flow tritium removal facility, as well as the three-loop and two-loop FHR systems were performed.

5.1 Cost analysis of the cross-flow tritium removal facility

To obtain an overall understanding of the cost of the tritium removal facility, a preliminary economic analysis was performed. The capital cost and operating cost were calculated. The operating cost was calculated for a time span of ten years with a 2% inflation rate per year considered. The annual inflation rate was estimated using the average values during the past ten years. The annual inflation rate each year was calculated using the monthly Consumer Price Index published by the Bureau of Labor Statistics (BLS) [32].

Table 5.1 Annual inflation rate 2006 – 2015 [32]

Year	Annual inflationrate [%]
2006	3.2
2007	2.8
2008	3.8
2009	-0.4
2010	1.6
2011	3.2
2012	2.1
2013	1.5
2014	1.6
2015	0.1
Average	2.15

For the economic analysis of the tritium removal facility, since its geometry resembles a cross-flow heat exchanger, the model developed for heat exchangers economic analysis [33] is used. In this model, the total cost consists of the capital cost and operating cost. Capital cost includes both material cost and fabrication cost. For the operating cost, a base cost is calculated and each year's operating cost is obtained by applying operating time related factors and inflation factors to the base cost.

Each heat exchanger has a fixed cost related to the total heat transfer surface area. For the tritium removal facility, it is the mass transfer surface area. The fixed cost C_b is calculated by:

$$C_b = \exp\left[8.202 + 0.01506\log A + 0.06811\left(\log A\right)^2\right] \tag{27}$$

where A is the total heat transfer surface area in the heat exchanger.

The fabrication cost of a heat exchanger is related to the type of the heat exchanger built. The tritium removal facility resembles a fixed head heat exchanger, of which the fabrication cost F_d is expressed as:

$$F_d = \exp\left(-0.9003 + 0.0906 \log A\right) \tag{28}$$

The pump work to compensate for the pressure drop varies with different pressure drop range, as listed in Table 5.2.

Table 5.2 Expressions of pressure cost

Operating pressure range [kPa]	Pressure cost expression
700 – 2100	$F_p = 0.8955 + 0.04981 \log A$
2100 – 4200	$F_p = 1.2002 + 0.0714 \log A$
4200 – 6200	$F_p = 1.4272 + 0.12088 \log A$

In the original model developed by Taal et al. [33], several common materials for heat exchanger fabrication are investigated. The material cost for each material is shown in Table 5.3.

Table 5.3 Expressions of material cost in year 2003

Material	Material cost expression
Stainless steel 316	$F_m = 1.4144 + 0.23296 \log A$
Incoloy 600	$F_m = 2.4103 + 0.50764 \log A$
Incoloy 825	$F_m = 2.3665 + 0.49706 \log A$
Hastelloy	$F_m = 3.7614 + 1.51774 \log A$

For the evaluation of the cross-flow tritium removal facility, the construction material is stainless steel 316H. To calculate the material cost, an adjustment is made by multiplying the ratio of average market prices of two materials at two years, i.e., 2003 and 2016. Take stainless steel 316H for example, which is used in the tritium removal facility for current research, the stainless steel 316/316L surcharge is as shown in Table 5.4 when the model was first used in 2003. The average price of stainless steel 316/316L in 2003 and 2016 has a ratio of 0.60. This ratio is also taken into consideration since it could potentially represent the market price change of the main structural material of the tritium removal facility.

Table 5.4 Historical surcharge of stainless steel 316/316L [34]

Month	1	2	3	4	5	6	7	8	9	10	11	12	Average
Year 2003	0.1583	0.1556	0.2097	0.2525	0.2608	0.2377	0.2804	0.3198	0.3109	0.3552	0.3970	0.4526	0.28
Year 2016	0.4112	0.4155	0.4003	0.4190	0.4333	0.4918	0.5090	0.5427	0.5819	0.5433	0.0000	0.0000	0.47

Economy situation varies from year to year. So a time factor is also added to the cost to take inflation into account. The annual inflation rate which is calculated before is adopted as the estimated time factor [32].

$$F_{yr} = 1.02 \tag{29}$$

The total capital cost is:

$$C_{capital} = C_b F_d F_p F_m F_{yr} \tag{30}$$

Energy cost C_E is required for the calculation of the operating cost. An estimated average market electricity cost of 10 cent/kW-h is adopted [35].

$$C_E = 0.1 \tag{31}$$

The pumping power is a main contribution to the operating cost. It is estimated as:

$$P = \frac{1}{\eta}\frac{\dot{m}}{\rho}\Delta p \tag{32}$$

where,

η is the pump efficiency, which is estimated to be 0.7 in this economic analysis;
$\dot{m}$ is the mass flow rate of molten salt on the shell side of the tritium removal facility;
ρ is the density of molten salt;
Δp is the pressure drop of molten salt flowing through the tritium removal facility.

Assuming other cost is much smaller than the pumping power cost, the operating cost can be expressed as:

$$C_{operating} = PC_E H \tag{33}$$

where H is the number of operation hours per year. In this economic analysis, 7000 hr/yr is used.
The final total cost is the addition of the capital cost and the operating cost:

$$C_{total} = C_{capital} + C_{operating} \tag{34}$$

A MATLAB code was written to calculate the cost of the tritium removal facility for ten years. The results are listed in Table 5.5. The total cost is calculated for 10 years after construction. In this calculation, all primary salt flows through the tritium removal facility, which leads to a large facility tube number. The primary salt flow rate used is the same with that in the AHTR conceptual design [3].

Table 5.5 Cost of the tritium removal facility with full primary coolant flow

Fixed cost [$]	C_b	1.33×10^{6}
Fabrication cost factor	F_d	0.94
Pressure cost factor	F_p	1.35
Material cost factor	F_m	6.94
Yearly inflation factor	F_{yr}	1.02
Energy cost [$/kW-h]	C_E	0.1
Capital cost [$]	$C_{capital}$	1.19×10^{7}
Operating cost [$]	$C_{operating}$	9.60×10^{8}
Total cost (10 years) [$]	C_{total}	9.61×10^{9}

To make the tritium management more economically attractive, one practical method is to reduce the flow rate passing the tritium removal facility. Therefore, the facility size will consequently be reduced as well. If 10% of the total primary salt flow rate passes the tritium removal facility, the cost was calculated, as shown in Table 5.6 based on the above model. The total cost in 10 years after construction is also reduced to about 10% of the cost with 100% primary coolant flow. The tritium removal rate might be lower in the case of 10% flow rate compared to 100% flow rate if the tritium concentration level in the primary coolant is kept the same. This can be make up by raising the tritium concentration level in the primary loop, as discussed in previous sections.

Table 5.6 Cost of the tritium removal facility operating with 10% primary coolant flow rate

Fixed cost [$]	C_b	1.03×10^5
Fabrication cost	F_d	0.76
Pressure cost	F_p	1.24
Material cost	F_m	5.79
Yearly inflation factor	F_{yr}	1.02
Energy cost	C_E	0.1
Capital cost [$]	$C_{capital}$	1.19×10^7
Operating cost [$]	$C_{operating}$	9.60×10^7
Total cost (10 years) [$]	C_{total}	9.72×10^8

The cost evaluation of a double wall heat exchanger with tritium permeation barrier requires to know the amount of barrier needed. Yttrium, for instance, as a highly efficient tritium getter, its raw material unit price is $275/kg [36]. However, the estimation of the amount of yttrium required is complicated because the combination number of tritium to yttrium is subject to change with several factors, including temperature, pressure, probably also the geometry of yttrium, etc. Typical combination number is between 1 and 3. This makes the estimation difficult. For conservation, the combination number can be selected as 1, while 2 might be good for an average estimation.

The amount of yttrium required to absorb the permeated tritium is only one of the factors that influence the total required amount. Since it is reasonable to assume not all tritium will be absorbed immediately upon contacting with yttrium, an additional diffusion factor should be applied. To date, there is limited research on the influence of absorbed tritium, i.e., formation of yttrium hydride on the tritium absorption rate of yttrium. More research and investigation is needed for the estimation of yttrium amount in the double wall heat exchanger.

5.2 Two-loop FHR design based on the AHTR pre-conceptual design

In the AHTR preceonceptual design, the cooling system consists of three loops: the primary loop containing FLiBe, the intermediate loop containing KF-ZrF_4 and the power cycle containing water. The function of the intermediate loop is to transfer heat from the primary loop to the power cycle, and isolate the power cycle from the reactor block. The cooling system is shown in Figure 5.1.

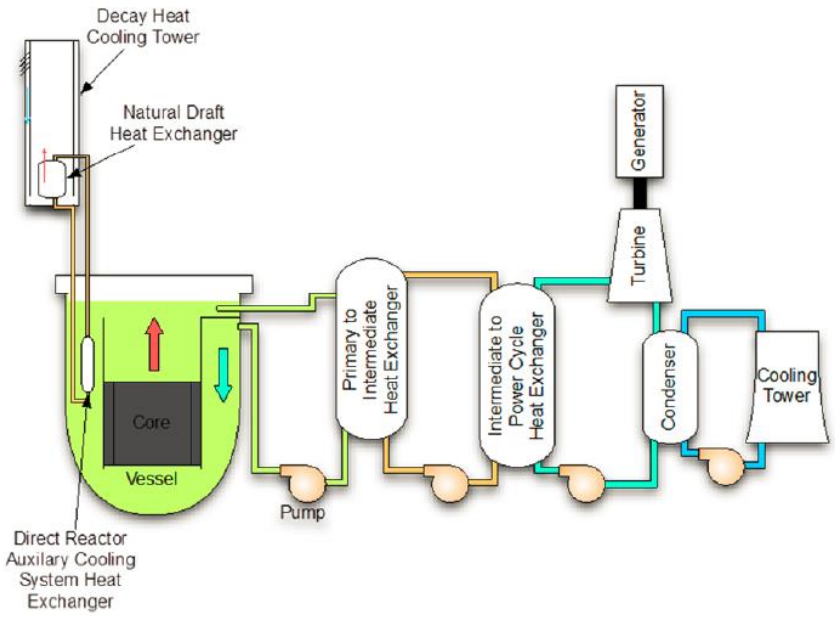

Figure 5.1 Cooling system of AHTR conceptual design [37]

With the tritium removal system designed for the primary loop, the function of the intermediate loop of preventing tritium from permeating into the power cycle is replaced. The intermediate loop can be eliminated for economic considerations. The primary loop will pass heat directly to the power cycle. The two-loop FHR design based on the AHTR conceptual design is shown in Figure 5.2.

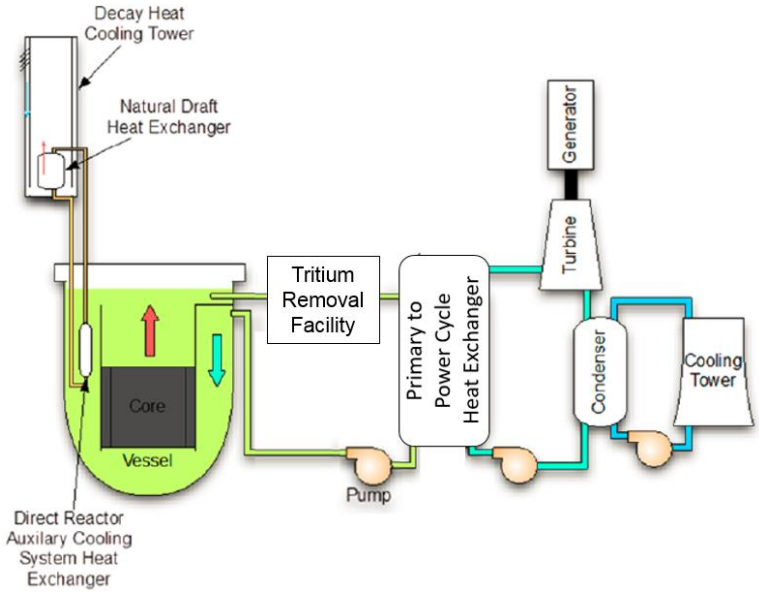

Figure 5.2 Two-loop FHR design

5.2.1 Comparison of different tritium control strategies

The strategies of tritium control in a two-loop FHR system are as follows:

1. The tritium removal facility;
2. The double wall heat exchanger [38];
3. The tritium removal facility and the double wall heat exchanger;
4. The tritium removal facility and tritium permeation barrier coatings;
5. The double wall heat exchanger and tritium permeation barrier coatings;
6. The tritium removal facility, the double wall heat exchanger and tritium permeation barrier coatings.

The cross-flow tritium removal facility or the double wall heat exchanger is the main facility in the tritium control system. It removes tritium from the system. Tritium permeation barrier coatings prevent tritium from permeating out of the system through structural materials. Coatings are necessary if the general tritium concentration in the primary loop is high. The higher the tritium concentration in the primary loop, the higher removal rate can be achieved in the main facility, but at the same time the higher the leakage rate from structural materials. So depending on the removal rate required and tritium concentration in the loop, one or more components can be incorporated in the tritium control system.

The cost of each strategy is shown in Table 5.7. For the tritium permeation barrier coatings, since the size of the AHTR loops are not available, the cost cannot be estimated. The cost of the double wall heat exchanger is estimated using the double wall NDHX. In the system, the intermediate heat exchanger is larger than the NDHX in size. Therefore, the cost of a double wall intermediate heat exchanger is higher than a double wall NDHX listed in the table. From the comparison, strategy 1 is the most economy among the six strategies.

Table 5.7 Cost comparison of tritium control strategies

Strategy number	Main facility	Capital cost [$M]
1	Tritium removal facility	11.9
2	Double wall heat exchanger	36.6 [38]
3	Tritium removal facility Double wall heat exchanger	48.5
4	Tritium removal facility Tritium permeation barrier coatings	11.9 plus cost of the tritium permeation barrier coatings
5	Double wall heat exchanger Tritium permeation barrier coatings	36.6 plus cost of the tritium permeation barrier coatings
6	Tritium removal facility Double wall heat exchanger Tritium permeation barrier coatings	48.5 plus cost of the tritium permeation barrier coatings

5.2.2 Comparison of two-loop and three-loop FHR systems

Comparing the two-loop design to the original three-loop design, the former does not have the entire intermediate loop but has a tritium removal facility installed on the primary loop. An

economic analysis is carried out to investigate whether the two-loop design is of advantages in the aspect of construction and operation cost.

The reference design of FHR in this project is the AHTR pre-conceptual design. Because this design is still in its early stage, not all the details have been determined. The size of the coolant loops, geometry or dimensions of the components, pumping power, etc. are not available yet. The available parameters of the intermediate loops in the AHTR pre-conceptual design are listed in Table 5.8 [37].

Table 5.8 Intermediate salt loops parameters

Parameter	Unit	Value
Salt material	-	$KF\text{-}ZrF_4$
Supply temperature	°C	675
Return temperature	°C	600
Flow rate	kg/s	43200
Pressure	-	Atmospheric
Number of loops	-	3
Pipe wall material	-	Hastelloy N

Due to the lack of design details, the following assumptions are made in the current economic analysis:

1. The amount of heat transfer fluids in the primary loops and the power cycle is the same in both the three-loop design and the two-loop design;
2. The cost of primary to power cycle heat exchanger in the two-loop design equals half of the cost of the two heat exchangers in the three-loop design. By reducing the intermediate loops, the cost of loop-coupling heat exchangers is reduced to half;
3. The cost of the main facility in the tritium control system equals the cost of a heat exchanger in the intermediate loop.

With the above assumptions, the main differences between the two designs are listed in Table 5.9. Because of the lack of the entire intermediate loop, the cost of the two-loop design does not include the salt, pump, piping of the intermediate loop. Additionally, the two heat exchangers that are required in the three-loop design can be reduced to one in the two-loop design. The two-loop design has the cost of tritium removal facility which is not included in the original three-loop design.

Table 5.9 Main differences between the two-loop and three-loop FHR designs

Two-loop design	Three-loop design
Tritium control system	Intermediate loops piping
	Intermediate loops pumps
	Intermediate loops salt ($KF\text{-}ZrF_4$)
	Intermediate to power cycle heat exchanger

The main component of the tritium control system is the tritium removal facility or the double wall heat exchanger. If the assumption that the cost of the main facility equals a heat exchanger is applied, then compare to the two-loop design, the three-loop design has the additional cost of the piping, pumps and salt. For the piping and the salt, it is mainly the construction cost. The cost of maintenance is relatively low. For the pumps, both the construction and the operation cost are major parts of the total cost. Therefore, both the construction and the operation cost of the three-loop design are higher than those of the two-loop design. The two-loop design FHR without the intermediate loop offers economic advantages compared to the original three-loop design.

6 Summary

Tritium generation is a potentially significant issue in advanced nuclear reactors, such as FHRs. To limit the leakage rate of tritium to the same level of a commercial PWR, a tritium control and mitigation system has been designed for advanced nuclear systems. The system consists of four main components, namely, redox control of the primary coolant, a cross-flow tritium removal facility, an intermediate heat exchanger (IHX) with double-wall design and tritium permeation barrier coatings applied to structural materials as necessary.

The redox control is a global chemical potential control in the entire primary loop. In the primary coolant, FLiBe, tritium generated can exist in two major forms, TF and T_2. The ratio of these two chemical forms changes with different chemical potential of the primary coolant. TF is corrosive to structural materials. Therefore, redox control is necessary to keep the amount of TF in the primary coolant at an acceptable range. Beryllium is selected as the redox control agent. With proper chemical potential in the primary coolant, the major existence form of tritium in the primary salt coolant will be T_2.

The cross-flow tritium removal facility is designed to increase the turbulence of the molten salt, and therefore, increase the tritium removal efficiency. The cross-flow tritium removal facility features a modular design to meet different demands of tritium removal rate at various power levels in an FHR plant. A tritium transport calculation method based on the logarithmic mean square root of the partial pressure difference has been developed, and a MATLAB code is written based on this method. The code calculation results are compared with the calculation results from a code using the finite volume method as well as experimental data of hydrogen permeation through a nickel tube, and the results agree well. Two validation experiments are designed with H_2 as the surrogate for T_2: one with molten salt FLiNaK as the fluid and solvent of H_2 and the other with reactor off-gas Kr as the fluid. For the experiment using the molten salt, due to the relocation of our research group and thus the delay of the construction of the molten salt loop, it is not yet set up. For the experiment using the off gas option, a laboratory-scale test loop was designed and set up at the University of Idaho. A small-scale cross-flow tritium removal facility that consists of 27 tubes in the tube bank was fabricated. However, due to the time constraint related to laboratory safety review and approval, the experiment has not been carried out at the writing of this report. Both experiments are planned to be carried out in the near future.

A double-walled IHX has been designed as a component of the tritium control and mitigation system. It is to be used together as the cross-flow tritium removal facility to minimize tritium leakage into the secondary (or intermediate) coolant through the large surface area of the IHX. In this IHX design, a sweep gas flows through the gaps between the two tube walls. Tritium in the primary salt coolant can permeate through the inner tube wall and be carried away by the sweep gas, and therefore, with a very small fraction leaking into the secondary coolant. At the same time, heat transfer resistance in the IHX is increased because of the added tube and sweep gas gap. An optimization between the heat transfer performance and the effective tritium permeation reduction is necessary when additional requirements and information become available.

To further minimize tritium leaking into the surrounding environment through the structural materials, tritium permeation barrier coatings can be applied as necessary. Tritium permeabilities of several candidates have been reviewed and it is found that Al_2O_3 is a promising material for this purpose. One limitation using tritium permeation barriers is that the barrier coating requires a high level of integrity. Cracks and other defeats of the coating will significantly reduce the ability of tritium permeation reduction. In practical operation, this could be an issue since the integrity of the coating may be challenging to maintain, especially at high temperatures.

A preliminary economic analysis has been carried out to study the construction and operating cost of the cross-flow tritium removal facility, as well as the cost comparison of the two-loop and three-loop FHR designs. For the cross-flow tritium removal facility, it is found that the operation cost can be lowered if a fraction of the primary coolant flow, instead of the entire primary coolant flow, is directed to flow through the tritium removal facility. The AHTR pre-conceptual design has been used as the prototype for the three-loop design. In the AHTR design, the intermediate loop functions as a buffer loop for tritium permeation from the primary loop to the power generation cycle loop. It is shown that with the elimination of the intermediate loop, the two-loop FHR design holds economic advantages over the original three-loop design.

References

[1] C.W. Forsberg, L.W. Hu, P.F. Peterson and K. Sridharan, "Fluoride-Salt-Cooled High-Temperature Reactors (FHRs) for Base-Load and Peak Electricity, Grid Stabilization, and Process Heat," Department of Nuclear Science and Engineering, Massachusetts Institute of Technology, Cambridge, MA, MIT-ANP-TR-147, 2012.
[2] D.F. Williams, "Assessment of candidate molten salt coolants for the advanced high temperature reactor (AHTR)," ORNL/TM-2006/12, ORNL, 2006.
[3] D.T. Ingersoll, "Status of preconceptual design of the advanced high-temperature reactor (AHTR)," ORNL/TM-2004/104, ORNL, 2004.
[4] P. Sabharwall, H. Schmutz, C. Stoots and G. Griffith, "Tritium production and permeation in high-temperature reactor systems," *Proceedings of the ASME 2013 Heat Transfer Summer Conference*, American Society of Mechanical Engineers, 2013.
[5] S. Fukada, A. Morisaki, A. Sagara and T. Terai, "Control of tritium in FFHR-2 self-cooled FLiBe blanket," *Fusion Engineering and Design* **81**, pp. 477-483, 2006.
[6] Fukada, S., Y. Edao, S. Yamaguti and T. Norimatsu, "Tritium recovery system for Li–Pb loop of inertial fusion reactor," *Fusion Engineering and Design* **83**, pp. 747-751, 2008.
[7] D.W. Green and R.H. Perry, *Perry's Chemical Engineers' Handbook* (7th ed.), New York: McGraw-Hill, 1997.
[8] R.E. Buxbaum, "The use of zirconium-palladium windows for the separation of tritium from the liquid metal breeder-blanket of a fusion reactor," *Separation Science and Technology* **18**, pp. 251-1273, 1983.
[9] C. Hsu and R.E. Buxbaum, "Palladium-catalyzed oxidative diffusion for tritium extraction from breeder-blanket fluids at low concentrations," *Journal of Nuclear Materials* **141**, pp.238-243, 1986.
[10] P. Calderoni, P. Sharpe, M. Hara and Y. Oya, "Measurement of tritium permeation in FLiBe ($2LiF–BeF_2$)," *Fusion Engineering and Design* **83**, pp. 1331-1334, 2008.
[11] A.P. Malinauskas and D.M. Richardson, "The solubilities of hydrogen, deuterium, and helium in molten Li_2BeF_4," *Industrial & Engineering Chemistry Fundamentals* **13**, pp. 242-245, 1974.
[12] R.A. Anderl, S. Fukada, G. R. Smolik, R. J. Pawelko, S. T. Schuetz, J. P. Sharpe and B. J. Merrill, "Deuterium/tritium behavior in FLiBe and FLiBe-facing materials," *Journal of Nuclear Materials* **329**, pp. 1327-1331, 2004.
[13] S. Fukada and Akio Morisaki, "Hydrogen permeability through a mixed molten salt of LiF, NaF and KF (Flinak) as a heat-transfer fluid," *Journal of Nuclear Materials* **358**, pp. 235-242, 2006.
[14] Y. Zeng, L. Du, S. Wu, Y. Qian, G. Wang, Y. Huang, H. Zhu and W. Liu, "Permaability of hydrogen in molten salt FLiNaK (LiF-NaF-KF)," *Nuclear Energy Science and Engineering* **38**, No. 2, 2015.
[15] H.D. Röhrig, R. Hecker, J. Blumensaat and J. Schaefer, "Studies on the permeation of hydrogen and tritium in nuclear process heat installations," *Nuclear Engineering and Design* **34**, pp. 157-167, 1975.
[16] COMSOL, "Packed bed reactor", http://www.comsol.com/model/packed-bed-reactor-238, accessed on 01/01/2017.
[17] A.P. Fraas and M. N. Özışık, *Heat Exchanger Design*, New York: Wiley, 1965.

[18] H-K. Chung and A. Dalgarno, "Diffusion of hydrogen atoms in helium gas and helium atoms in hydrogen gas," *Physical Review A* **66**(1), 2002.
[19] http://demonstrations.wolfram.com/BinaryDiffusionCoefficientsForGases/.
[20] T.R. Marrero and E.A. Mason, "Gaseous diffusion coefficients," *Journal of Physical and Chemical Reference Data* **1**, pp. 3-118, 1972.
[21] R.E Treybal, *Mass-Transfer Operations*, New York: McGraw-Hill, 1980.
[22] L.H. Gevantman, "Solubility of selected gases in water," *Nitric Oxide (NO)* **308**(3), 2000.
[23] http://www.engineeringtoolbox.com/gases-solubility-water-d_1148.html.
[24] B. Jähne, G. Heinz and W. Dietrich, "Measurement of the diffusion coefficients of sparingly soluble gases in water," *Journal of Geophysical Research: Oceans* **92**(C10), pp. 10767-10776, 1987.
[25] Q. Lv, H.C. Lin, I.H. Kim, X. Sun, R.N. Christensen, T.E. Blue, G. Yoder, D. Wilson and P. Sabharwall, "DRACS Thermal Performance Evaluation for FHR," *Annals of Nuclear Energy* **77**, pp. 115-128, 2015.
[26] M. Wang, J. Song, X. Wu, X. Tan, B. Meng and S. Liu, "Metallic nickel hollow fiber membranes for hydrogen separation at high temperatures," *Journal of Membrane Science* **509**, pp. 156-163, 2016.
[27] T.R. Marrero and E.A. Mason, "Gaseous Diffusion Coefficient," *Journal of Physics Chemistry Reference Data*, 1(1), 1972.
[28] COMSOL, Separation through dialysis, https://www.comsol.com/model/membrane-dialysis-258, accessed on 01/01/2017.
[29] Y. Kwon, *Handbook of essential pharmacokinetics, pharmacodynamics and drug metabolism for industrial scientists*, Springer Science & Business Media, 2001.
[30] https://en.wikipedia.org/wiki/Partition_coefficient#cite_note-1, accessed on June 30, 2017.
[31] S.K. Lee, Y.G. Ohn and S.J. Noh, "Measurement of Hydrogen Permeation through Nickel in the Elevated Temperature Range of 450–850°C," *Journal of the Korean Physical Society*, 10(63), pp. 1955-1961, 2013.
[32] http://www.usinflationcalculator.com/inflation/current-inflation-rates/, accessed on 01/01/2017.
[33] M. Taal, I. Bulatov, J. Klemeš and P. Stehlík, "Cost estimation and energy price forecasts for economic evaluation of retrofit projects," *Applied Thermal Engineering*, **23**(14), pp. 1819-1835, 2003.
[34] https://www.atimetals.com/businesses/ATIFlatRolledProducts/Tools/Pages/Surcharge-History.aspx.
[35] https://www.statista.com/statistics/183700/us-average-retail-electricity-price-since-1990/.
[36] http://www.pcreml.com/rare-earth-pricing.
[37] V.K. Varma, D.E. Holcomb, F.J. Peretz, E.C. Bradley, D. Ilas, A.L. Qualls and N.M. Zaharia, "AHTR mechanical, structural, and neutronic preconceptual design," ORNL/TM-2012/320, Oak Ridge National Laboratory, 2012.
[38] S. Zhang, S. Shi, X. Wu, X. Sun and R. Christensen, "Double-Wall Natural Draft Heat Exchanger Design for Tritium Control in FHRs," *Proceedings of the 25th International Conference on Nuclear Engineering (ICONE-25)*, Shanghai, China, 2017.